Journal of Materials Science & Technology 209 (2025) 262–291

Contents lists available at ScienceDirect

Journal of Materials Science & Technology

journal homepage: www.elsevier.com/locate/jmst

Review Article

Laser shock processing of titanium alloys: A critical review on the microstructure evolution and enhanced engineering performance

Qian Liu[a], Shuangjie Chu[a,b], Xing Zhang[c], Yuqian Wang[d], Haiyan Zhao[a,e], Bohao Zhou[a], Hao Wang[f], Genbin Wu[g], Bo Mao[a,*]

[a] School of Materials Science and Engineering, Shanghai Jiao Tong University, Shanghai 200240, China
[b] Baoshan Iron & Steel Cooperation Limited, Shanghai 201900, China
[c] School of Mechanical and Electric Engineering, Soochow University, Suzhou 215100, China
[d] Department of Mechanical Engineering, University of Nevada-Reno, Reno 89557, USA
[e] Baowu Special Metallurgy Cooperation Limited, Shanghai 201900, China
[f] Shanghai Engineering Research Center of Laser Intelligent Manufacturing, Shanghai Institute of Laser Technology Co., Ltd., Shanghai 200233, China
[g] Department of Orthopaedic Surgery, Shanghai General Hospital, Shanghai Jiao Tong University School of Medicine, Shanghai 200080, China

ARTICLE INFO

Article history:
Received 12 February 2024
Revised 27 April 2024
Accepted 29 April 2024
Available online 31 May 2024

Keywords:
Laser shock peening
Titanium alloys
Microstructure evolution
Mechanical properties

ABSTRACT

Titanium (Ti) and its alloys are frequently utilized as critical components in a variety of engineering applications because of their high specific strength and excellent corrosion resistance. Compared to conventional surface strengthening technologies, laser shock peening (LSP) has increasingly attracted attention from researchers and industries, since it significantly improves the surface strength, biocompatibility, fatigue resistance, and anti-corrosion ability of Ti and its alloys. Despite numerous studies that have been carried out to elucidate the effects of LSP on microstructural evolution and mechanical properties of Ti and its alloys in recent years, a comprehensive review of recent advancements in the field of Ti and its alloys subjected to LSP is still lacking. In this review, the standard LSP and the novel process designs of LSP assisted by thermal, cryogenic, electropulsing and magnetic fields are discussed and compared. Microstructural evolution, with focuses on the dislocation dynamics, deformation twinning, grain refinement and surface amorphization, during LSP processing of Ti alloys is reviewed. Furthermore, the enhanced engineering performance of the LSP-processed (LSPed) Ti alloys, including surface hardness, wear resistance, fatigue life and corrosion resistance are summarized. Finally, this review concludes by presenting an overview of the current challenges encountered in this field and offering insights into anticipated future trends.

1. Introduction

Titanium (Ti) and its alloys have been widely utilized as structural materials in a variety of engineering applications, owing to their high specific strength [1], excellent corrosion resistance, superior biocompatibility [2,3], and outstanding fracture toughness [4,5]. These exceptional material properties have facilitated their extensive deployment in a range of applications including aircraft engines [3], steam turbine blades [6], bio-implants [7], and petrochemical facilities [8], as shown in Fig. 1. During their operational lifespan, Ti and its alloys are often subjected to various deleterious factors such as corrosion, stress corrosion, friction and wear, cyclic loading, leading to the potential failure of mechanical components. Therefore, it is of critical importance to develop advanced material processing approaches to further improve their engineering performance.

Surface processing techniques have shown great potency in enhancing the overall engineering performance of metallic components due to their high flexibility without affecting the structural integrity. Over the past decades, various metal surface processing techniques have been developed, such as shot peening (SP) [9–11], ultrasonic SP (USP) [12,13], ultrasonic rolling (UR) [14–17], surface mechanical attrition treatment (SMAT) [18–20], and ultrasonic nanocrystal surface modification (UNSM) [21–23]. During these processes, the material microstructure is tailored by high-strain-rate plastic deformation, leading to enhanced surface hardness, corrosion resistance, and fatigue durability. For example, Wen et al. [11] showed that the fatigue limit of Ti64 alloy was improved by 20% from 485 MPa to 580 MPa after SP processing. Kumar et al.

* Corresponding author.
E-mail address: bmao@sjtu.edu.cn (B. Mao).

https://doi.org/10.1016/j.jmst.2024.04.075
1005-0302/

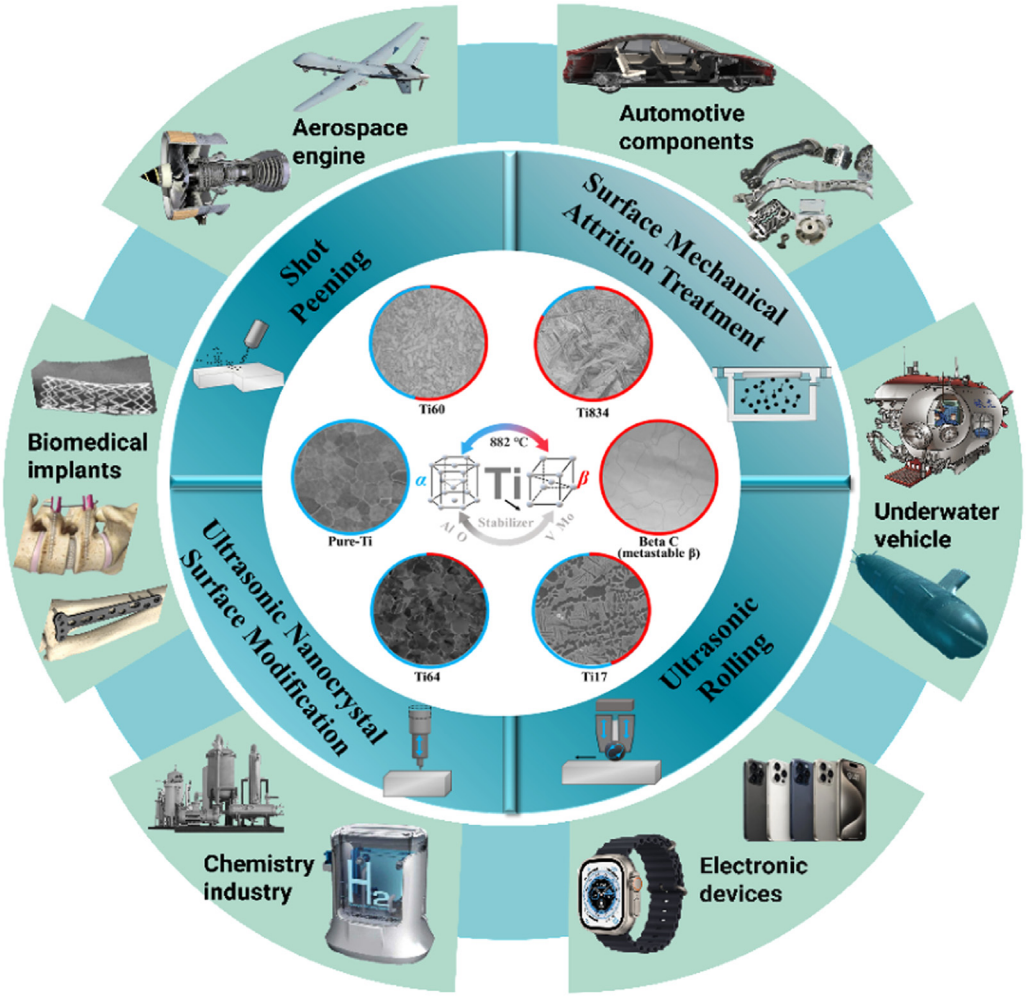

Fig. 1. Typical classification, surface processing techniques, and applications of Ti alloys.

[12] found that the low cycle fatigue life of Ti13Nb13Zr alloy was improved threefold by USP. Liu et al. [15] showed that the fatigue limit of Ti64 alloy was ~39% higher for UR-processed sample (695 MPa) than that for the unprocessed sample (500 MPa). Singh et al. [20] reported that the wear rate of Ti64 alloy was decreased from 3.23×10^{-4} mm^3/Nm to 2.51×10^{-4} mm^3/Nm by SMAT. Amanov et al. [23] found the width of the fretting wear scars of Ti64 alloy could be significantly decreased from 680 μm to 630 μm after UNSM treatment. However, these traditional surface processing techniques are gradually becoming inadequate to meet the evolving demands of high-performance component production and processing, due to the limited depth of introduced compressive stress layer [24], increased surface roughness and formation of microcracks [25].

In addition to the aforementioned surface strengthening techniques, laser shock peening (LSP) has emerged as a promising material processing approach and has gained considerable attention in recent years. LSP was firstly developed in the 1970's by Anderholm [26] to improve the fatigue life of engine blades and has been widely utilized in plenty of industrial applications nowadays. Our previous research has shown that LSP is capable of improving the surface hardness [27,28], wear resistance [29,30], corrosion resistance [31,32], and even stretch formability [33,34] of metallic materials. Compared with SP, USP, and SMAT, LSP stands out due to the following advantages: (1) larger depth of introduced compressive residual stress (CRS), (2) higher shockwave pressure resulting in prominent grain refinement and surface strengthening effect, (3) higher flexibility with controllable process parameters. Therefore, LSP has been widely employed to enhance the durability of Ti-based components, particularly those featured by complex geometries and high yield strength [24].

Due to its scientific significance and practical applications, extensive research efforts have been paid to the investigation of microstructure evolution and engineering performance of Ti and its alloys processed by LSP [35–39]. For instance, Zhang et al. [40] found the fatigue strength of Ti64 at 2×10^6 cycles was enhanced to 264 and 306 MPa after single-impact LSP and two-impact LSP, respectively, which were 22.2% and 41.7% higher than those of the unprocessed sample (216 MPa). Hua et al. [41] investigated the hot corrosion behavior of TC11 alloy treated by LSP. The result showed the average corrosion rate at 650 °C after LSP processing was 4.56 (mg/(cm^2 h)), 78.5% lower than that of the untreated sample (21.22 mg/(cm^2 h)). Zhang et al. [40] found the microhardness of the as-received Ti64 was improved by 15% and 24% after single-impact LSP and two-impact LSP, respectively. The improved surface hardness [42], fatigue strength [43], fatigue life [44] and resistance to crack propagation [45] after LSP treatment can be mainly ascribed to the introduced CRS [46] and surface microstructural change [47,48], including dislocation accumulation [49], grain refinement [50], deformation twinning [51] and phase transformation [52].

It is evident that a thorough review of LSP process design, along with its impacts on the microstructural evolution and mechanical properties of metallic materials, is crucial not only for optimiz-

ing the LSP process but also for its practical applications. Up to now, several review articles related to LSP have been published. For instance, Montross et al. [53] reviewed the influence of LSP on the residual stresses and mechanical properties of metal alloys. Deng et al. [54] reviewed LSP-induced microstructural evolution and mechanical property enhancement of metallic materials and alloys with summarizing the relationship between the mechanical properties and LSP processing parameters. Praveenkumar et al. [55] reviewed the surface properties of aeroengine materials under different LSP controlling parameters. Kalainathan et al. [56] reviewed the application of LSP without coating (LPwC) on ferrous, aluminum and Ti alloys. Liao et al. [57] reviewed the relationship among process design, microstructure evolution and mechanical performance of metallic material processed by warm LSP (WLSP). These review efforts have provided valuable insights into the optimization of the microstructure and corresponding mechanical properties of LSP-processed metallic materials. Compared with metals with a cubic crystal structure, such as aluminum alloys and steels, the plastic deformation mode of most Ti alloys is significantly different due to their hexagonal close-packed (HCP) structure with low symmetry and limited availability of slip systems. Moreover, Ti alloys with different alloying compositions result in a variety of phases, which exhibit distinct plastic deformation mechanisms. Therefore, the microstructure response and strengthening mechanism of Ti alloys subjected to LSP may be significantly different from aluminum alloys and steels. Moreover, Ti alloys with multiple phases may exhibit distinct plastic deformation modes due to the complex strain and stress partition behavior during ultra-high strain rate plastic deformation. However, particular efforts focusing on the summary of Ti alloys subjected to LSP approach have yet to be undertaken.

Given the rapid advancements in both research and practical applications of LSP on Ti alloys, the timeliness and significance of conducting a comprehensive review to consolidate recent developments in this field become apparent. The goal of the work is to provide a thorough analysis of the latest advancements in the effects of LSP on Ti and its alloys. In this paper, an extensive examination of LSP and field-assisted LSP is undertaken, followed by the comprehensive review of the microstructure evolution during LSP of Ti alloys including the dislocation motion, deformation twinning, phase transformation, grain refinement and surface amorphization. Moreover, the enhanced engineering performances of LSPed Ti alloys such as compressive residual stress (CRS), surface hardness, wear resistance, fatigue life and corrosion resistance are discussed. Finally, this review summarizes the existing challenges and proposes potential avenues for future research endeavors regarding LSP treatment of Ti and Ti alloys. Henceforth, the main goal of this review is to provide important insights and guidance for the design of novel surface-strengthening techniques and address the research gap by assessing various microstructural characteristics and engineering performances of Ti and its alloys treated by LSP.

2. LSP process design and working principle

As an emerging surface modification technology, LSP is commonly adopted to tailor the surface properties of Ti and its alloy. In recent years, the increasing severity of extreme environments has posed significant challenges to LSP as a single mechanical-field action. Hence, several novel LSP technologies have been proposed. On the basis of surrounding temperature LSP can be classified as WLSP and Cryogenic LSP (CLSP). Moreover, external-filed assisted LSP technology is the key development direction of LSP technology with the introduction of new energy fields, such as electric, and magnetic fields. These new developments in LSP technology have different working principles, offering unique and significant benefits. This section will delve into the working principles of both conventional and new LSP technologies.

Even if LSP and related novel laser processing techniques have shown promise in enhancing the engineering performance of Ti and its alloys, there remains a significant need for further investigation. The future of research in this field is crucial for advancing the industrial applications of these techniques. Key objectives for future research include: Establishing comprehensive process simulation and material models; Exploring additional enhancement of engineering performances; Advancing novel laser processing methods. In summary, further research is imperative to unlock full industrial applicability of several novel LSP technologies.

2.1. Standard LSP

As schematically illustrated in Fig. 2(a), the standard LSP process involves the utilization of a high-energy pulsed laser to irradiate the target surface. An absorbing layer is typically placed on the top of the target to act as an ablative coating, while a transparent confinement is subsequently applied over this ablative coating. During the LSP process, the high-energy (GW/cm^2) short-pulse (ns) laser beam travels through the transparent confinement and irradiates the ablative coating, resulting in an instantaneous vaporization and ionization of the coating layer. This leads to the formation of high-temperature-high-pressure plasma, which expands swiftly away from the target surface. Due to the presence of transparent confinement, the expanding plasma is trapped and re-directed towards the surface, leading to the generation of a high-pressure shockwave (GPa) propagating within the target material. Based on the widely accepted Fabbro's LSP model [58], the peak shockwave pressure P of the laser-induced plasma is defined by shock impedance Z (confining media Z_1 and target material Z_2) and the laser intensity $I(t)$:

$$\frac{2}{Z} = \frac{1}{(Z_1 + Z_2)} \tag{1}$$

$$\frac{\mathrm{d}L(t)}{\mathrm{d}t} = \frac{2}{Z}P(t) \tag{2}$$

$$I(t) = P(t)\frac{\mathrm{d}L(t)}{\mathrm{d}t} + \frac{3}{2\alpha}\frac{\mathrm{d}}{\mathrm{d}t}[P(t) * L(t)] \tag{3}$$

where L is the length of the plasma interface, α is the ratio of the thermal energy to the internal energy of the plasma (in the 0.3–0.5 range). $Z_1 = Z_{\mathrm{glass}} = 1.44 \times 10^6 \mathrm{g/(cm^2\ s)}$, $Z_2 = Z_{\mathrm{Ti64}} = 2.33 \times 10^6 \mathrm{g/(cm^2\ s)}$ [59]. $I(t)$ is given by Eqs. (4) and (5):

$$I_0 = \frac{Q}{\pi\left(d/2\right)^2 \Delta t} \tag{4}$$

$$I(t) = I_0 \frac{1}{\sigma\sqrt{2\pi}} \mathrm{e}^{-\frac{1}{2}\left(\frac{t-\mu}{\sigma}\right)^2} \tag{5}$$

where I_0 is the maximum laser intensity, Q is the pulse laser energy, d is the beam diameter, and Δt is the laser pulse duration. The value of σ can be estimated from the effective laser duration FWHM (full width at half maximum), where $\mathrm{FWHM} = 2\sqrt{2\ln 2}\sigma \approx 5$ ns, and $\mu = 6\ \sigma$. Based on Eqs. (1)–(5), the temporal evolution of shockwave pressure for various laser intensities is calculated as shown in Fig. 2(b). It can be seen that the shockwave pressure in LSP experiments rapidly reaches a peak value (GPa) within 20 ns and then decays gradually over time. As the shockwave propagates into the Ti block, the effective pressure decays with the increase of depth. Once the shockwave pressure exceeds the metal's Hugonoit elastic limit (HEL), which is defined by the magnitude of elastic precursor of the shock wave and is related to yield strength σ_y

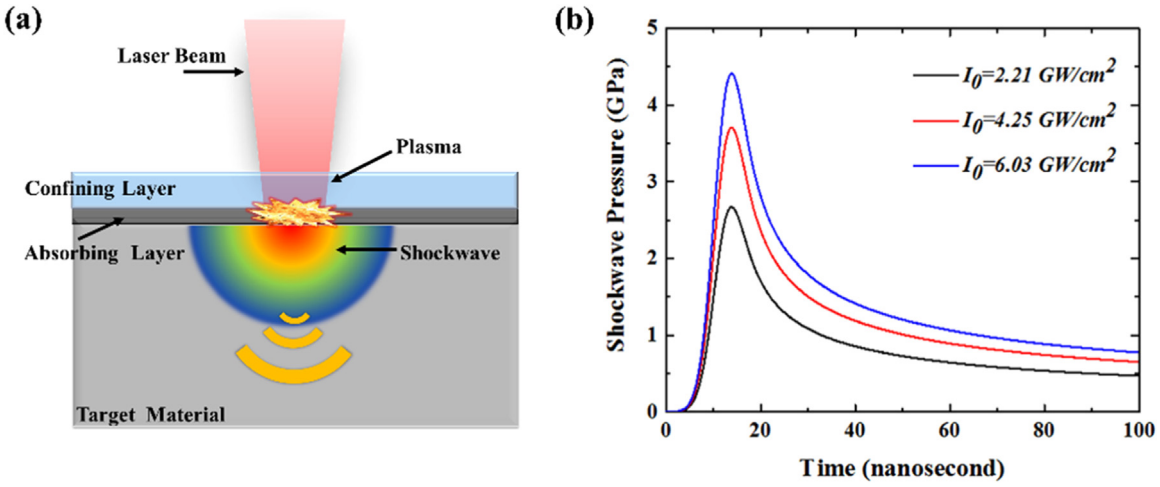

Fig. 2. (a) Schematic view of the LSP experimental setup. (b) The temporal evolution of laser shockwave pressure as affected by the laser intensity in LSP experiments, estimated by Fabbro's model. Reproduced from Ref. [27] with permission of the publisher (Elsevier).

and Poisson's ratio ν of the material through HEL $= \frac{1-\nu}{1-2\nu}\sigma_y$, the high-strain-rate plastic deformation occurs underneath the irradiated region, accompanied by the grain refinement and induction of CRS. The degree of grain refinement from the matrix to the surface includes low-density dislocations, dense dislocations (or dislocation line entanglement), DWs (dislocation walls), DCs (dislocation cells), sub-grain boundaries, and nanocrystals. The gradient dislocation movement induced the formation of gradient structure. Notably, the thickness of the CRS field formed by LSP can reach 1 to 2 mm, which is nearly 5 to 10 times deeper than that by SP [60].

Under LSP processing, the strengthening effect of Ti and its alloys is primarily influenced by the pressure of the shock wave, with plastic deformation occurring only when the shockwave pressure exceeds the metal's Hugoniot elastic limit. The duration of the laser pulse affects the depth of strengthening, as the shock wave gradually attenuates during propagation. Based on Eqs. (3) and (4), the pressure of the shockwave is influenced by laser intensity, pulse laser energy, laser pulse duration and beam diameter. The spot geometry, overlap ratio, and number of shock impacts also have a great influence on the degree of plastic deformation. Furthermore, the strengthening effect also depends on the initial microstructure features, such as grain size, phase constitution, and crystallographic of Ti and its alloys.

2.2. Warm LSP

Despite that the depth and magnitude of CRS in materials can be significantly enhanced by LSP, this technique suffers from stress relaxation under cyclic loading (especially at high temperatures), owing to the monotonic and cyclic relaxation. In order to stabilize the microstructure and superior mechanical properties after LSP, a novel approach named WLSP was developed by the research group of Cheng et al. [61] in 2010 on the basis of thermo-mechanical coupling effect, as schematically depicted in Fig. 3(a). WLSP is a technique that controls the strain-induced microstructures using thermal effects, which takes advantages of both LSP and dynamic strain aging (DSA). The temperature range of DSA of Ti alloys can be calculated by the model proposed by Qian et al. [62,63]:

$$T_{\text{upper}} = \frac{-Q_{\text{m}}}{k\ln\left(a^2/12D_0\right)} \tag{6}$$

$$T_{\text{lower}} = \frac{-u_{\text{m}}}{k\ln\left(a_0/c_{\text{s}}\right)}, \tag{7}$$

where T_{uper} and T_{lower} are the upper limit and the lower limit of the dynamic strain aging temperature, respectively. Q_{m} is the activation energy for the partial polymerization of solute atoms, a is lattice constant, k is Boltzmann constant, D_0 is diffusion coefficient, u_{m} is the energy of the maximum interaction between the dissolved atoms and dislocation, a_0 and c_{s} are the average and maximum concentration of solute elements in an alloy, respectively. Therefore, it can be deduced that the temperature range of the dynamic strain aging of Ti alloys is approximately 0.2–0.5 of its melting point, i.e., Ti alloys are generally heated to a range of 150–350 °C during WLSP.

The processing temperature during WLSP is a critical parameter that affects the enhancement of mechanical properties. Pan et al. [64] investigated the effects of processing temperature on the CRS distribution and microstructure of Ti64 processed by WLSP (WLSPed). As shown in Fig. 3(b), the peak CRS continuously reduced with increasing temperature and considerably dropped at temperatures above 300 °C, whereas the width and depth of the CRS region were increased with increasing temperature. 300 °C has higher affected width and depth of the CRS than other WLSPed samples. The CRS and surface microhardness of Ti64 processed by WLSP at 300 °C could be significantly improved by 36.2% and 5% respectively, compared to the counterparts processed by standard LSP. 300 °C was decided as the optimal peening temperature for our WLSPed Ti64 alloy. Another difference between WLSP and LSP is the degree of grain refinement. More intense grain refinement was found in WLSPed sample due to the multiplication of dislocations and deformation twins, than their LSPed counterparts (Fig. 3(c, d)). Moreover, an amorphous layer was found in the WLSPed Ti64 alloy, as shown in Fig. 3(e, f). Closed to the amorphous–nanocrystalline interface, many finer nanocrystalline grains were found (Fig. 3(e, f)). Zhou et al. [65] analyzed the effects of processing temperature during WLSP of Ti64 alloys on CRS and fatigue performance. The CRS region in the sample processed by WLSP at 300 °C was found to be 725 μm in depth and 14.6 mm in width, while the LSPed sample exhibited a CRS depth of 540 μm and width of 13.2 mm. During low-cycle fatigue (LCF) tests, the final axial displacement of WLSPed specimens at 300 °C (3.413 mm) is increased by 14% in comparison to LSPed samples (3.002 mm).

2.3. Cryogenic LSP

Besides the warm processing technique, cryogenic treatment is also a special heat treatment method, which is conducive to

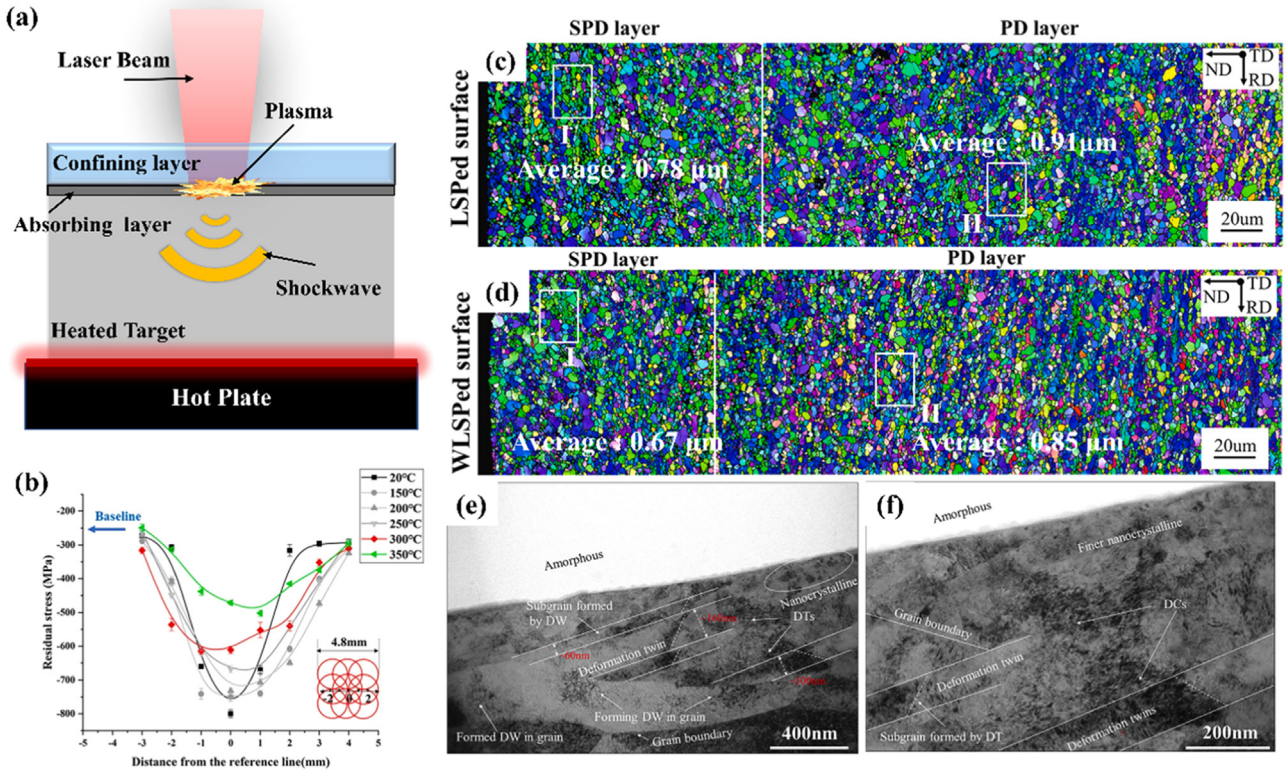

Fig. 3. (a) Schematic illustration of WLSP process, (b) surface CRS distributions of the WLSPed samples at different processing temperatures. Cross-sectional microstructure of the Ti64 alloys processed by (c) LSP and (d) WLSP. (e, f) TEM images showing the cross-sectional microstructure of the Ti64 alloy after WLSP at 300 °C. Reproduced from Ref. [64] with permission of the publisher (Elsevier).

the formation of deformation nano-twins (NTs) and stacking faults (SFs) [66–68]. CLSP combines the dual advantages of cryogenic temperature and ultra-high strain rate deformation to perform a synergistic strengthening treatment on the materials' surface, which was firstly proposed by Ye et al. [69] in 2011. The schematic view of the CLSP process as shown in Fig. 4(a). In the CLSP process, the target material is typically placed in a container filled with liquid nitrogen, leading to a distinctive microstructure evolution that differs from that observed in the LSPed sample. Li et al. [67] investigated the effect of CLSP on the microstructure and mechanical properties of pure Ti and the results are shown in Fig. 4(b–f). It can be seen that the surface micro-hardness of CLSP processed (CLSPed) sample increased by 6.1% as compared to that of LSPed sample. EBSD (electron backscatter diffraction) characterization of the surface microstructure demonstrated that the proportion of twin boundaries was increased by 133.3% for the CLSPed sample, as shown in Fig. 4(c, d). Further examination of the near-surface area by transmission electron microscopy (TEM) revealed that in comparison to LSPed sample, a higher density of dislocation structures and interlacing of mechanical twins (MTs) were found in CLSPed sample (Fig. 4(e, f)), owing to the suppression of the motion and slip of dislocation structures under cryogenic temperature. For TC6 alloys, Li et al. [66] found that the tensile strength, elongation and micro-hardness of the sample processed by CLSP at −130 °C were increased by 6.1%, 6.6% and 4.86% respectively, than that of LSPed sample. The main reasons for the significant improvements in properties are as follows: (1) the formation of higher density of dislocations and deformation twins; (2) accumulation of dislocation on both sides of the twin boundaries. Li et al. [70] studied the high-cycle bending fatigue behavior of TC6 alloy under LSP and CLSP. Compared with the LSPed sample, the damping ratio and fatigue life of CLSPed specimen was increased by 15.4% and 32.94%, respectively.

2.4. LSP assisted by external field

External field has long been employed to assist the deformation and control of the microstructure of metallic materials since the discovery of electro-plastic effect and magneto-plastic effect [71,72]. Compared with thermal heating, electropulsing is a promising method that can improve material ductility [73], heal cracks [74] and optimize the material microstructure and texture [75,76]. Dong and his team [77] proposed an electric field-assisted LSP (EPLSP) process that induces electro-plasticity effect by pulsed current.

The schematic view of the EPLSP process is depicted in Fig. 5(a). An electropulsing generator is used in the EPLSP pretreatment experiment. A copper electrode with a chrome-plated surface is connected to the two ends of the sample. In the EPLSP process (Fig. 5(a)), the sample is subjected simultaneously to LSP treatment and a pulsed current. They found the hardness of Ti64 alloy was increased with the peak current density for EPLSP treatment (Fig. 5(b)), despite that the maximum temperatures for the different electrical parameters were similar (Fig. 5(c)). It was also demonstrated that in comparison to the continuous current-assisted LSP (CCLSP), EPLSP contributed to a higher surface hardness, indicating that the pulsed current exhibited a more significant impact on the material plasticity than the thermal effect. The EBSD results revealed a higher density of dislocations in the EPLSPed sample than that in the LSPed and CCLSPed samples (Fig. 5(d–f)). This outcome was ascribed to the enhanced dislocation mobility induced by the electropulsing process [77]. The surface roughness of the samples before and after LSP treatment was characterized by a 3D surface profiler. The results showed that this electro-plastic effect also resulted in a greater surface roughness after EPLSP (~0.30 mm) than that after LSP (~0.05 mm), as shown in Fig. 5(g). The increase of surface roughness in EPLSPed may lead

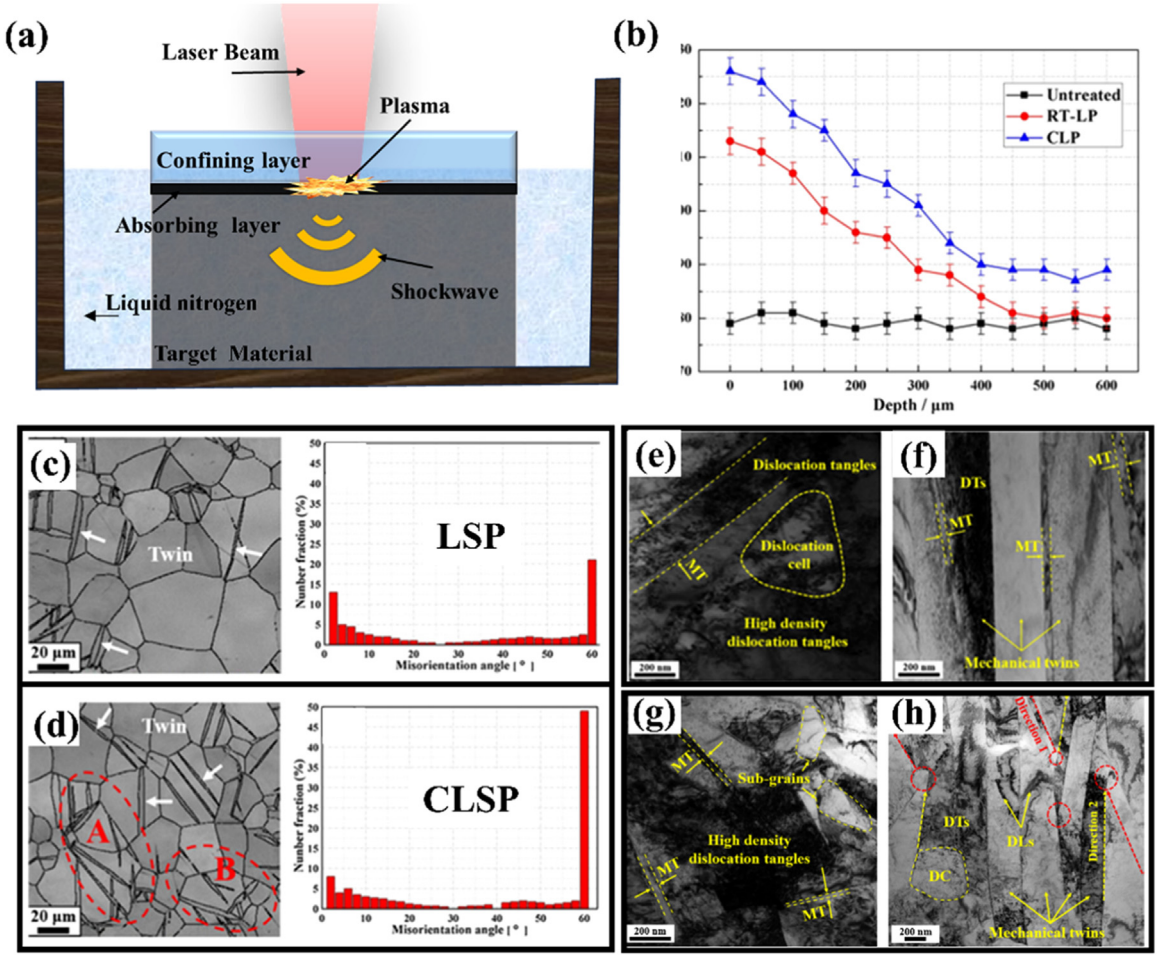

Fig. 4. (a) Schematic illustration of CLSP process. (b) In-depth micro-hardness distribution of pure Ti processed by LSP and CLSP. EBSD analysis for the pure Ti processed by (c) LSP and (d) CLSP on the near-surface layer. TEM images at a depth of 20 μm below the top surface by (e, f) LSP, (g, h) CLSP. Reproduced from Ref. [67] with permission of the publisher (Elsevier).

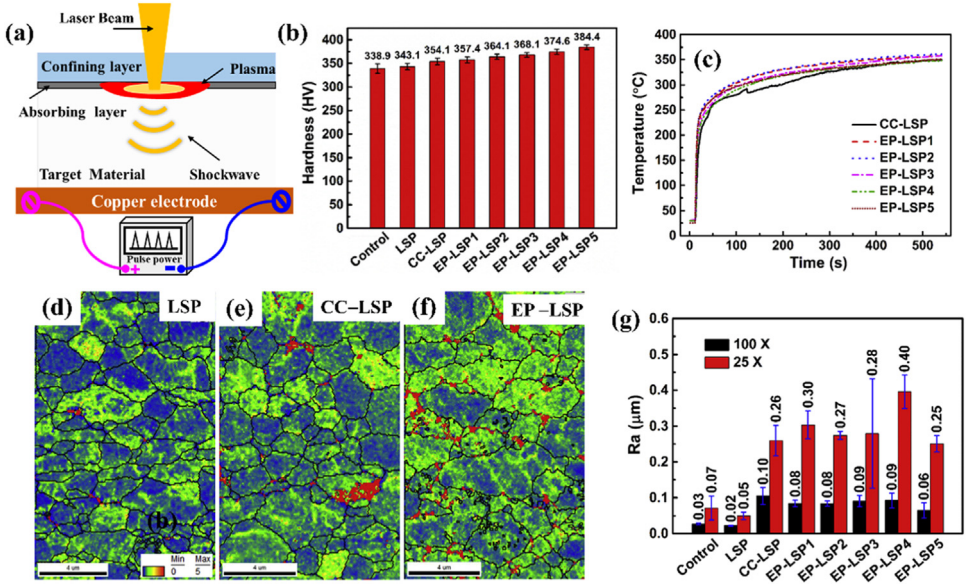

Fig. 5. (a) Schematic view of EPLSP process. (b) Surface hardness of the samples processed by LSP, CC-LSP, and EPLSP treatments. (c) Temperature history for samples processed by CC-LSP and EPLSP. KAM maps of the Ti64 samples processed by (d) LSP, (e) CC-LSP and (f) EPLSP. (g) Surface roughness changes after different treatments. Reproduced from Ref. [77] with permission of the publisher (Elsevier).

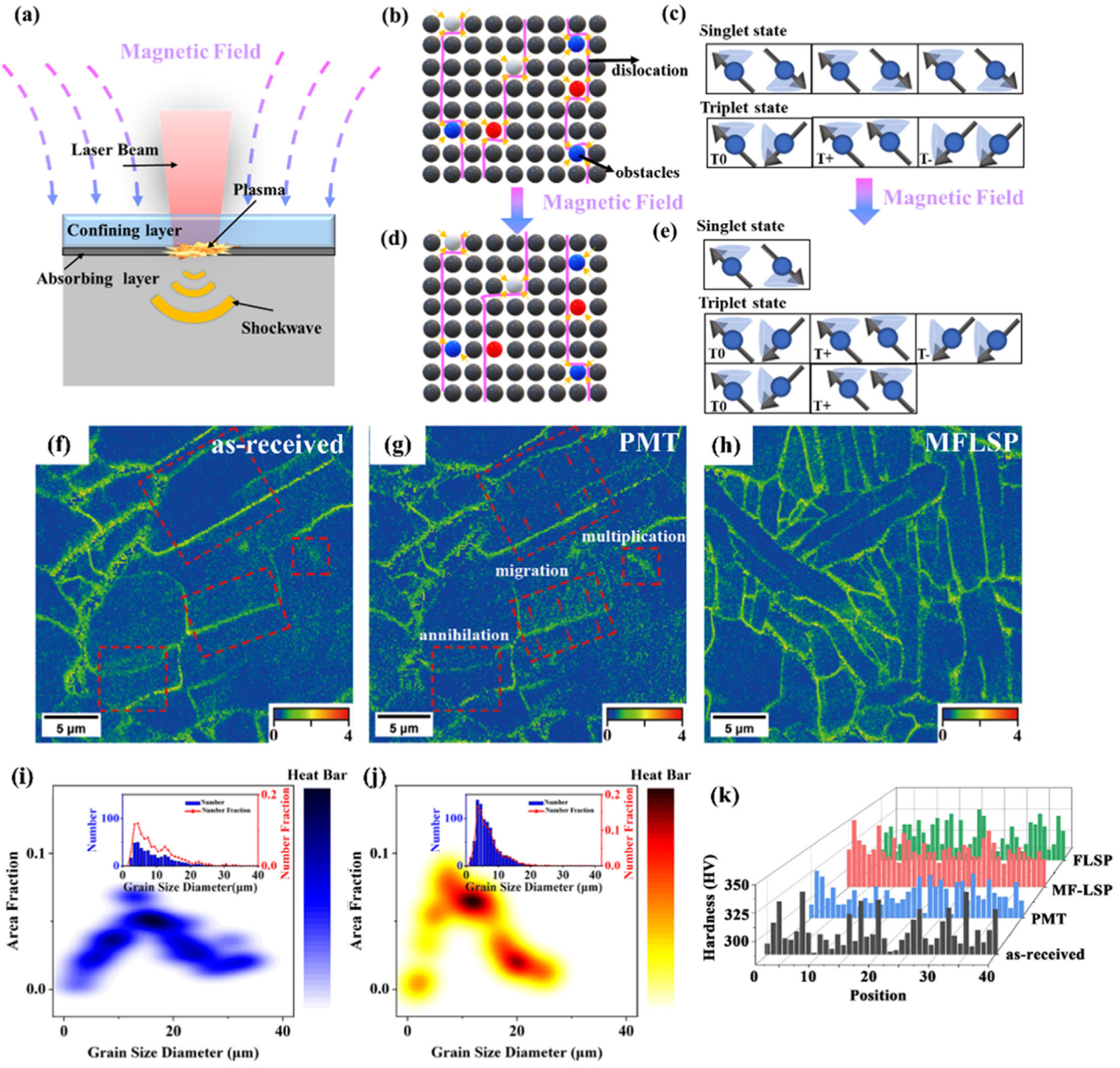

Fig. 6. (a) Schematic view of MFLSP. (b) The obstacles' pinning and (c) the orbital spin coupling effect. (d) The obstacles' pinning and (e) the orbital spin coupling effect after external magnetic field excitation. KAM mappings of (f) as received, (g) PMTed, and (h) MFLSPed samples. Heat maps of the grain size distribution for the (i) as received, (j) MFLSPed. (k) Histograms of surface hardness in different positions. Reproduced from Ref. [80] with permission of the publisher (Wiley).

to local stress concentration compared to the smooth surface of the unLSPed specimen (~0.03 mm) [78]. Nevertheless, the change of roughness after LSP has minimal impact on the hardness, fatigue durability, and corrosion resistance. In essence, the beneficial effects of the LSP-induced high-level CRS and gradient microstructures (grain refinement, twin and dislocation) are much greater than the negative effects of increased surface roughness [43,78,79].

In addition to the electropulsing, magnetic fields have been explored as an adjunct to LSP process, leading to the development of magnetic field-assisted LSP (MFLSP) as proposed by He et al. [80], depicted in Fig. 6(a). This technique utilizes a half-sine-wave pulsed magnetic field generated by a pulse current in the Pulse magnetic field treatment (PMT). Under a non-magnetic field condition, as shown in Fig. 6(b), the movement of dislocations is hindered by pinning effects resulting from the Coulomb interaction between dislocations and obstacles. Meanwhile, the orbital spin exists in a resonance coexistence zone, fluctuating between singlet and triplet states (Fig. 6(c)). The introduction of an external magnetic field contributes to dislocation depinning and dislocation multiplication (Fig. 6(d)). This effect is caused by the influence of magnetic field on the state of orbital spin, facilitating a transition from the singlet state to the triplet state (Fig. 6(e)). In the triplet state, the binding energy between the dislocation and the obstacles is reduced compared to the singlet state, making dislocations more likely to de-pin from the obstacles [81].

As an example case, He et al. [80] investigated the effects of MFLSP on dislocation motion, grain size, and surface hardness of Ti64 alloys. Fig. 6(f–h) presents the KAM maps for semiquantitative description of the distribution of total dislocation density. In comparison to the as-received sample, the PMTed sample exhibited a lower KAM value, indicating the weakened crystal distortion rate and misorientation due to the disaggregation of dislocations in the LAGBs. The MFLSPed sample presented a higher KAM value, indicating severe plastic deformation caused by laser-induced DRX.

Moreover, MFLSP promoted the multiplication of more dislocations and the stacking of new dislocations, facilitating the uniform grain refinement of Ti64 alloys. The grain size distribution maps indicated that in comparison to the as-received sample (Fig. 6(i)), the preferred clustering points in MFLSPed sample were reduced to one main point (10–20 μm) and one additional point (~20 μm). Additionally, based on the inset images, it was measured that the fraction of small diameter grains (<10 μm) was increased by 159.57% by MFLSP processing. Furthermore, the uniform grain refining effect contributed to the homogeneity of surface hardness values and surface strengthening effect (surface hardness increased by 18.21 HV), as shown in Fig. 6(k).

3. Microstructural Evolution

Understanding the microstructural evolution of Ti alloys during LSP is of critical importance for process design and optimization. However, Ti alloys demonstrate a diversity of phases influenced by their alloying compositions. Beyond the two dominate allotropic phases, hexagonal close-packed structured $\alpha-\mathrm{Ti}$ and body-centered cubic structured $\beta-\mathrm{Ti}$, additional phases such as $\alpha'-\mathrm{Ti}$, $\alpha''-\mathrm{Ti}$, $\omega-\mathrm{Ti}$ also present. These phases exhibit distinct plastic deformation mechanisms, resulting in different microstructural responses including dislocation movement [82,83], deformation twinning [51,67], phase transformation [84], grain refinement [47,50,85], and surface amorphization [48,86]. Moreover, LSP induces plastic deformation with an ultrahigh strain rate of $\sim 10^6$/s, during which the microstructural responses might be significantly different from those observed in quasi-static deformation. Table 1 summarizes the typical microstructure evolution features of Ti alloys after LSP process. The mechanism responsible for the individual feature will be discussed in this section.

3.1. Dislocation evolution

One significant aspect of microstructural evolution of Ti alloys subjected to LSP is the formation of high-density dislocations due to the high shockwave pressure [93]. In order to quantitatively assess the dislocation densities, Kernel average misorientation (KAM) conducted with EBSD date was applied to quantitatively calculate the dislocation densities [51]. TEM analysis was also performed to assess the dislocation structures present beneath the processed surface [87]. KAM conducted with EBSD date was applied to calculate the dislocation densities quantitatively. Sun et al. [60] showed that the dislocation density of the surface of Ti17 alloy was increased from 4.43×10^{13} m^{-2} to 1.10×10^{14} m^{-2} after LSP processing. Huang et al. [51] quantitatively estimated the geometrically necessary dislocations (GND) density at different depths within a Ti alloy subjected to three times LSP. It was measured that the dislocation densities at the surface, 400 μm depth and 950 μm depth were 5.1×10^{14}, 2.1×10^{14}, and 3.4×10^{14} m^{-2}, respectively, indicating the decreasing of GND densities with increasing depth from the peened surface.

High shockwave pressure and severe plastic deformation facilitate dislocation slip, then result in grain refinement [49]. Fig. 7 shows the grain refinement mechanism dependent on dislocation movements. There are mainly three states: (I) Laser shockwave triggers the dislocation slip, leading to a large accumulation of dislocation lines and the formation of DTs (dislocation tangles). (II) With the increasing time of shockwave, the high-density dislocations start to rearrange, inducing the formation of the dislocation cells and sub-grain boundaries. (III) Through continuous energy injection and dynamic recrystallization, the pile-up dislocations arranged into the sub-grain boundaries, further induced the formation of nanocrystalline. The surface nano-crystallization can enhance the surface hardness. Different states of dislocation movement at different depths induced the formation of a gradient structure, resulting in a gradient distribution of hardness. Furthermore, the increased surface hardness could improve the fatigue life by inhibiting the microcrack initiation and growth. Dislocation multiplication also can improve the adhesion between the outer oxide layer and the substrate, which further enhances the corrosion resistance. Detailed mechanisms will be discussed in Section 4.

As mentioned before, the accumulation of dislocation networks will promote the formation of sub-grains in the LSPed samples. Lainé et al. [94] analyzed the formation process of sub-grains in surfaces processed by LSP. As shown in Fig. 8(a, b), a residual stress layer with a depth of 50 μm was found in LSPed Ti64 alloys. Moreover, some sub-grains were found in the LSPed Ti64 alloys (Fig. 8(c, d)). Most sub-grains with extremely low misorientation (< 0.5°), indicating that they primarily consist of cellular dislocation structures aimed at accommodating the strains induced by LSP. A continuous grain rotation induced the misorientation of sub-grains increased to 5°–6°. Some dislocation tangles and the directional arrays of planar dislocations with cellular structure were evident in Fig. 8(e–g), verifying that the accumulation of dislocations induced the formation of small sub-grains.

Due to the difficulties of measuring the dislocation density experimentally, large amounts of studies have attempted to approach the evolution of dislocations by muti-scale simulations. For instance, Wang et al. [83,95] investigated the relationship between the laser spot overlap ratio/laser power density and dislocation cell using three-dimensional finite element model. Fig. 9(a) shows the multiple dimple profiles on the LSPed surface at 50% and 75% laser

Table 1
Microstructure evolution features of LSP process of Ti alloys.

Materials	Laser intensity ($\mathrm{GW/cm^2}$)	Microstructure evolution features	Refs.
Ti64	3.2 and 7.2	Formation of gradient CRS layer and gradient dislocation structure.	[43]
Ti64	25	Formation of $\{10\bar{1}2\}$ twins and poorly-developed dislocation boundaries.	[87]
Ti64	4.42	Multiply dislocations and deformation twins; More intense grain refinement.	[64])
Ti64	4.42	Formation of high dense shear bands to a depth of 200 mm.	[88]
Ti64	10.6	α' martensites refined by dislocation structures and MTs.	[89]
Ti834	9.4	Formation of sub-grain and dislocation cell, twin-matrix lamellae.	[90]
Pure Ti	14.1	Grain refined by multi-directional MTs-MTs intersections and secondary MTs-DWs intersections.	[50]
Pure Ti	–	Phase transformation	[84]
Ti17	3.9	Formation of the ω phase.	[91]
Ti17	10.6	Grain refinement by DTs (dislocation tangles) and deformation twins.	[2]
TB10	6.6	Dislocation tangled and distributed near the phase boundary; Formation of an amorphous layer.	[48]
TC21	10.86	Formation of SFs, dislocations, and sub-grains; phase transformation	[92]
TC6	10.6	Surface amorphization	[86]

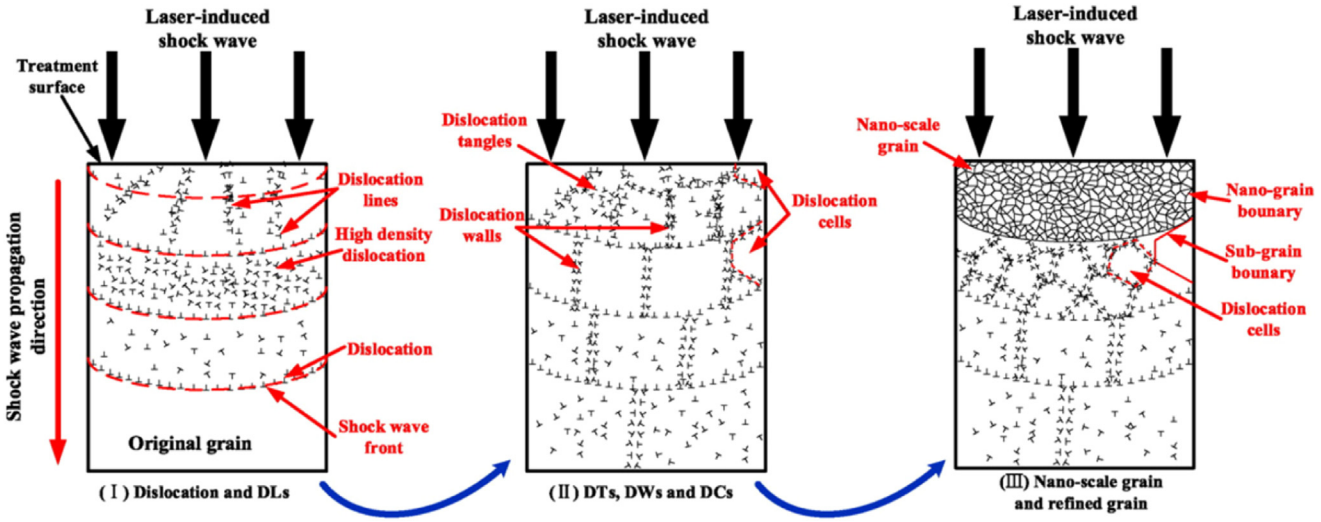

Fig. 7. Schematic illustration showing dislocation evolution process of TC6 alloys processed by LSP. Reproduced from Ref. [49] with permission of the publisher (Elsevier).

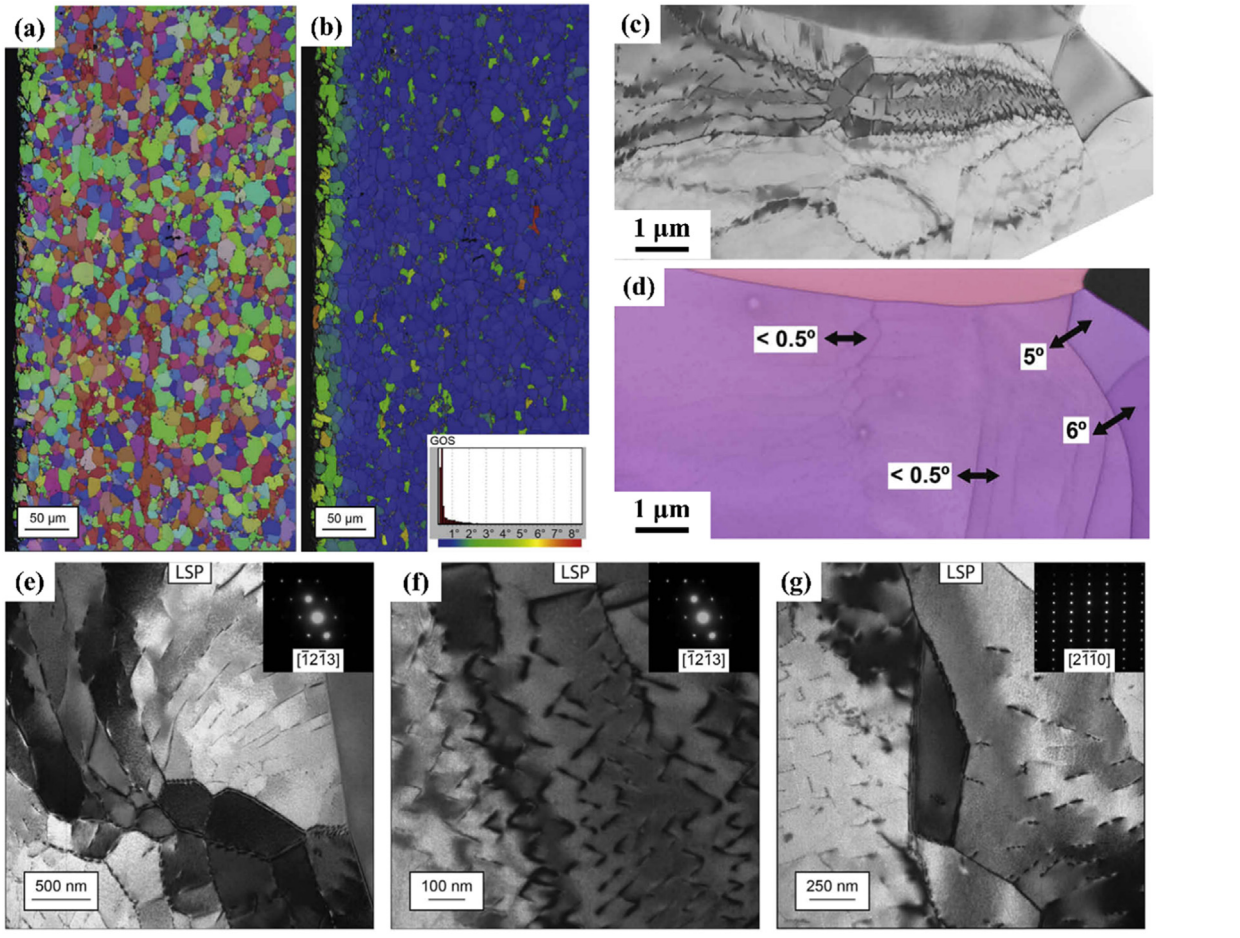

Fig. 8. (a) Inverse pole figure and (b) grain orientation spread map of the LSPed Ti64 alloys. (c) Lower magnification bright field TEM micrograph of sub-grains, (d) EBSD inverse pole figure color image of low angle sub-grain boundaries in sample. (e–g) Dislocation structure analysis in the sample. Reproduced from Ref. [94] with permission of the publisher (Elsevier).

spot overlap ratios. As shown in Fig. 9(b–d), under the same laser power density, the smaller in-depth dislocation cell sizes can be obtained by increasing the laser spot overlap ratio and laser shock wave pressures. Wang et al. [95] also found that the in-depth dislocation cell sizes decrease and tend to be saturated gradually with the increase of laser power density.

Besides finite element model, several studies have been carried out to investigate the dislocation dynamics in metallic materials processed by LSP via molecular dynamics (MD) simulation, which may provide more detailed information regarding the dislocation motion and accumulation. For instance, Gu et al. [96] investigated the evolution of dislocation in LSPed α – Ti by MD simulation. As

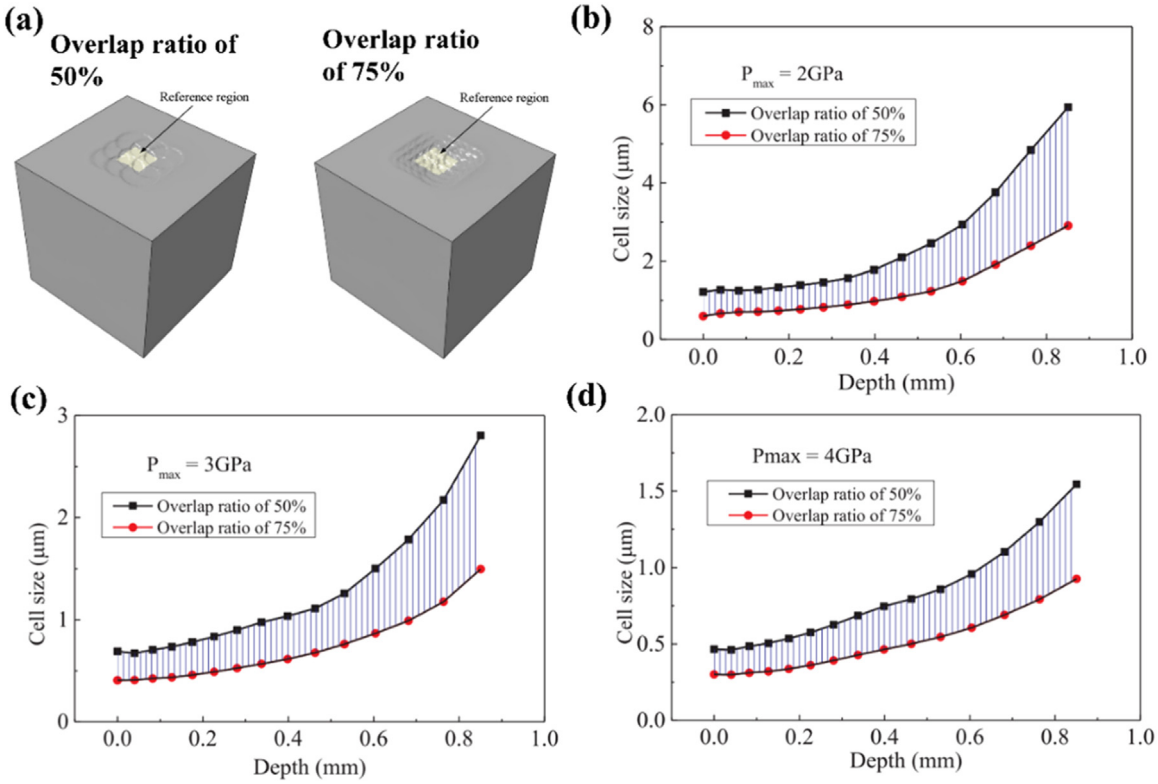

Fig. 9. (a) Surface indentations induced by LSP with different overlap ratios. Simulated results showing the effect of overlap ratio and shockwave pressure on the dislocation cell sizes of the sample: (b) P_{max} = 2 GPa, (c) P_{max} = 3 GPa, (d) P_{max} = 4 GPa. Reproduced from Ref. [83] with permission of the publisher (Elsevier).

shown in Fig. 10(a–c), the dislocation at the grain boundary moved along the impact direction as the propagation of shock wave front. With the increasing of impact time, the number of dislocation segments and total dislocation length also increased (Fig. 10(d, e)). Moreover, strain rate significantly affected the evolution trend of the dislocation atoms. Compared with the dislocation length induced by particle velocity of 0.5 km/s, the dislocation length under 1.5 km/s increased 87%. These results showed that the higher piston particle velocity induced the more formation of dislocation atoms at the same time (Fig. 10(d, e)).

Besides laser intensity and number of impacts, processing temperature significantly affects the dislocation multiplication ability during LSP. Pan et al. [64] showed that WLSP can activate more dislocation sources and multiplies the dislocation than LSP, due to the strong pinning effect on the dislocation movement during strain aging. Li et al. [67] found that CLSP is conducive to the suppression of dynamic recovery, thereby increasing the density and stability of dislocation structures. Compared to LSP, WLSP and CLSP demonstrate a more pronounced ability to induce dislocation multiplication.

3.2. Stacking faults evolution

The presence of stacking faults (SFs) in the ground state structure of a crystal is related to the stacking fault energy (SFE). SFs significantly influence dislocation motion and the formation of twins, thereby controlling the mechanical behavior of Ti alloys. In addition, $\alpha-$Ti and $\beta-$Ti have three independent slip systems and twelve independent slip systems [92], respectively, corresponding with low-level SFE and high-level SFE. Therefore, regulating the formation and distribution of SFs region in Ti alloys is significantly difficult. During the LSP process, some SFs were found in Ti alloys. He et al. [92] studied the effect of LSP on the formation of SFs in TC21 alloys. At the top surface to 300 μm deep in the TC21 alloy subjected to LSP, a large number of SFs was distributed at the boundary of twins (Fig. 11(a)). With the depth from the peened surface increasing, the SFs decreased until disappeared (Fig. 11(b)). As shown in Fig. 11(c–e), the formation of SFs was attributed to the $\alpha-$Ti transformation from HCP-Ti into $\beta-$Ti. Lou et al. [49] showed that SFs play an important role in the process of grain refinement and surface self-nanocrystallization of LSPed TC6 alloys.

3.3. Deformation twinning

Due to the low symmetry of hcp $\alpha-$Ti, twinning has been profusely observed in Ti and its alloys and plays a significant role during plastic deformation, particularly at a high-strain rate [51,67,92,94]. Deformation twinning is another critical characteristic in LSPed titanium alloys besides dislocation slip, which can accommodate plastic deformation and enhance mechanical properties. For example, the formation of twins divides parent grains and brings about a grain refinement effect, which improves the surface micro-hardness. Twinning also can inhibit the crack initiation by reducing the concentration of surface stress. Increasing twin boundaries facilitated the formation of passivation film, further enhancing the corrosion resistance. So far, six types of twins have been reported in Ti, including three types of tension twin (TTW) and three types of compression twin (CTW). The identification of different twinning types was carried out by EBSD analysis. Their misorientations angle/axis are summarized in Table 2. Schematic illustrations of the six twinning modes, including the twinning plane and crystallographic relationship are shown in Fig. 12.

Among these twinning modes, TTW1 and CTW1 twinning systems are the most commonly observed twining modes in Ti and its alloys processed by LSP due to their lower critical resolved shear stress. Previous studies have suggested that the formation of $\{10\bar{1}2\}$ twins in the $\alpha-$Ti is related to the dissociation of <a>

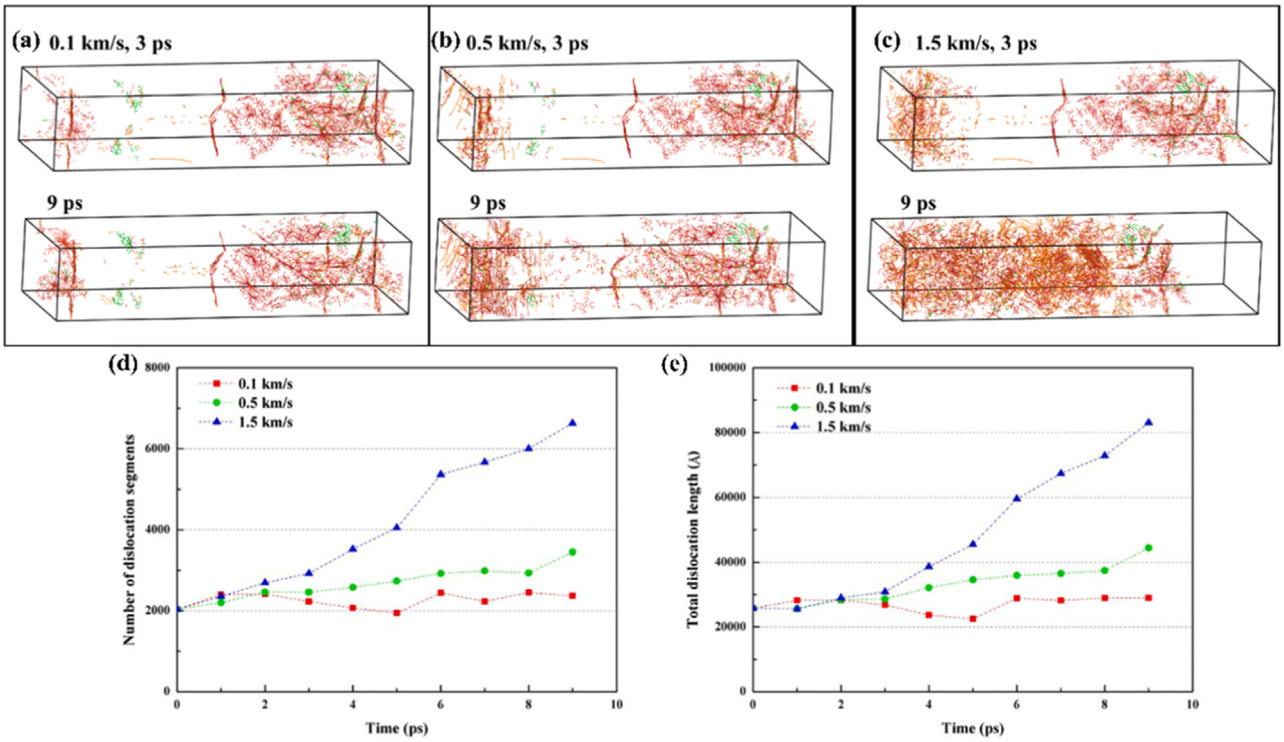

Fig. 10. Dislocation evolution induced by LSP at different times with piston particle velocities of (a) 0.1 km/s, (b) 0.5 km/s, and (c) 1.5 km/s. The variation of (d) the number of dislocation segments and (e) total dislocation length at different times. Reproduced from Ref. [96] with permission of the publisher (Elsevier).

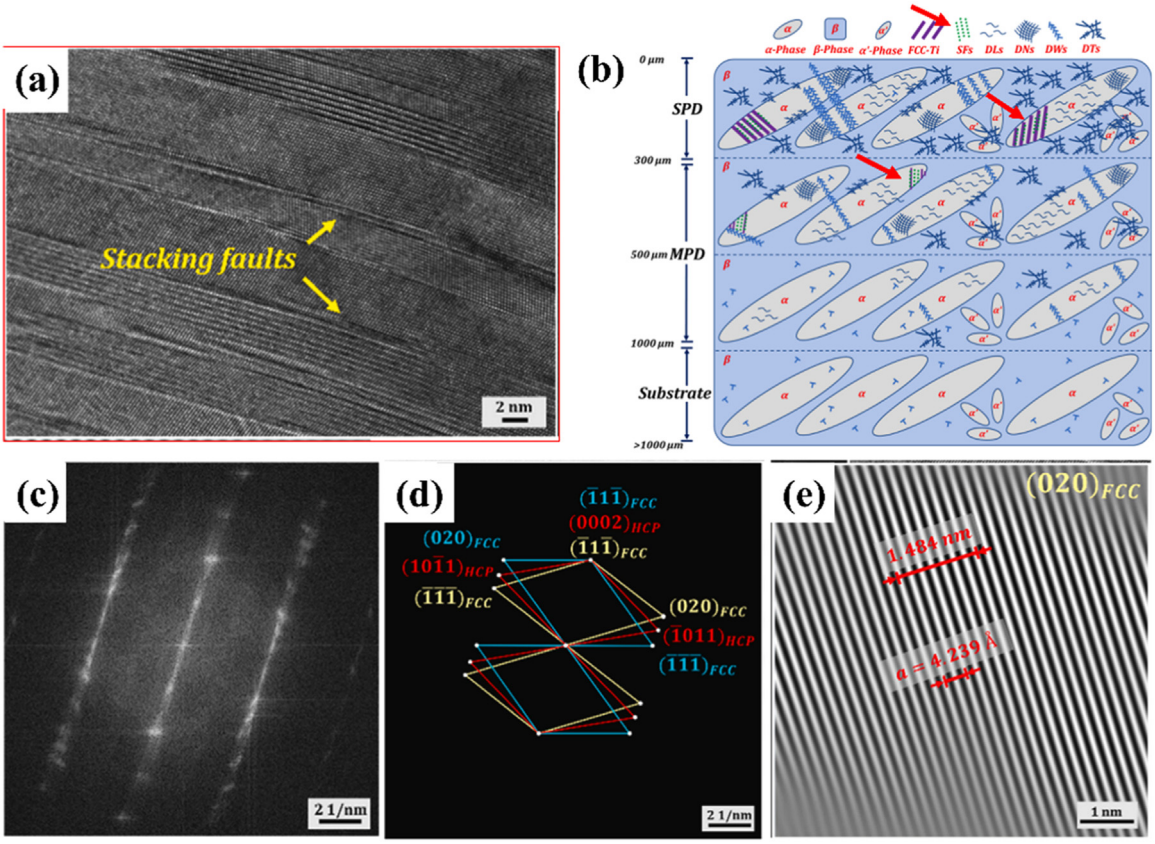

Fig. 11. (a) SFs structures in the surface of the TC21 alloy after LSP. (b) Schematic illustration of SFs evolution of TC21 alloy after LSP. (c) FFT image in (a). (d) Schematic diagram of diffraction spots in (c). (e) IFFT of (020) crystal plane of FCC-Ti. Reproduced from Ref. [92] with permission of the publisher (Elsevier).

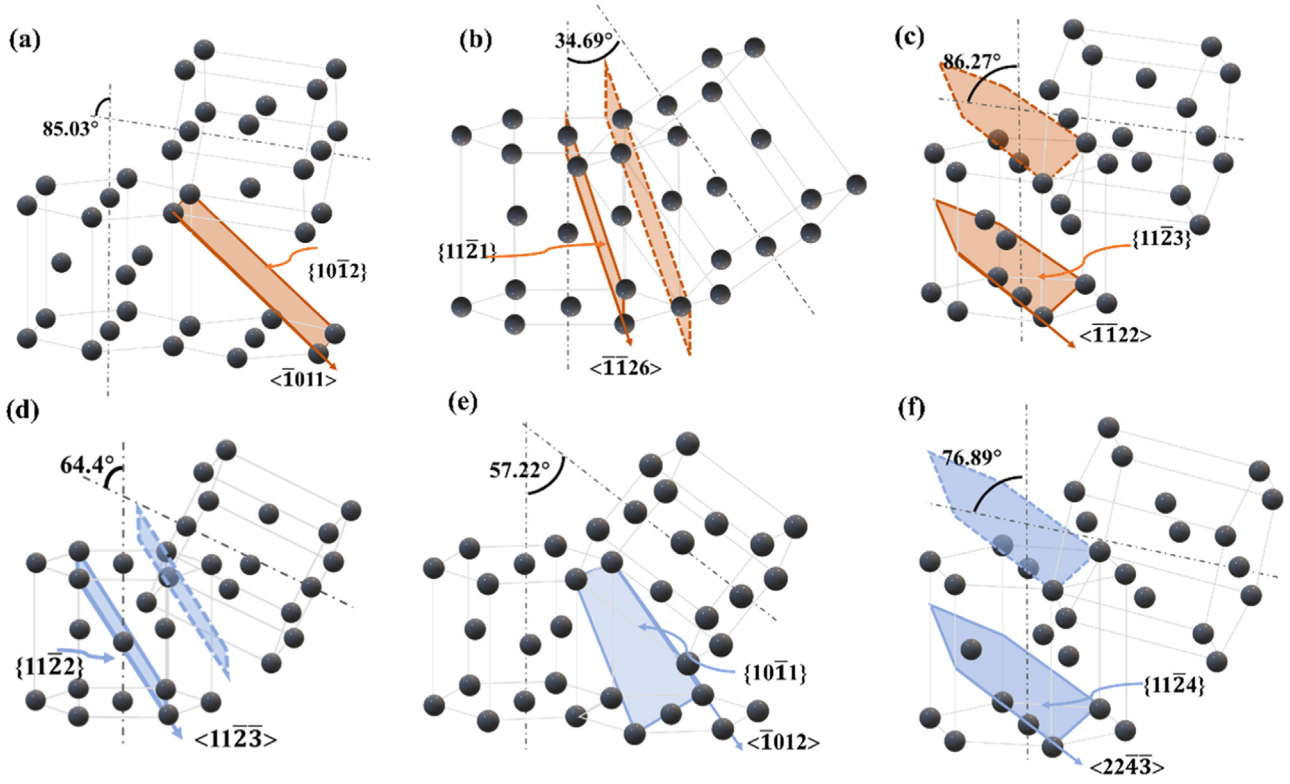

Fig. 12. Schematic illustration showing the crystallographic relationship between twin and parent in different twinning systems. Tension twin: (a) {10$\bar{1}$2}<$\bar{1}$011>, (b) {11$\bar{2}$1}<$\bar{1}\bar{1}$26>, (c) {11$\bar{2}$3}<$\bar{1}\bar{1}$22>. Compression twin: (d) {11$\bar{2}$2}<11$\bar{2}\bar{3}$>, (e) {10$\bar{1}$1}<$\bar{1}$012>, (f) {11$\bar{2}$4}<22$\bar{4}\bar{3}$>.

Table 2
Misorientation angle/axis of the commonly observed tension and compression twin systems in Ti. Reproduced from Ref. [97] with permission of the publisher (Elsevier).

Types of twins	Twinning system system	misorientation angle/axis
TTW 1	{10$\bar{1}$2}<$\bar{1}$011>	85.03° along (11$\bar{2}$0)
TTW 2	{11$\bar{2}$1}<$\bar{1}\bar{1}$26>	34.69° along ($\bar{1}$010)
TTW 3	{11$\bar{2}$3}<$\bar{1}\bar{1}$22>	86.27 ° along ($\bar{1}$010)
CTW 1	{11$\bar{2}$2}<11$\bar{2}\bar{3}$>	64.4 ° along ($\bar{1}$010)
CTW 2	{10$\bar{1}$1}<$\bar{1}$012>	57.22 ° along (11$\bar{2}$0)
CTW 3	{11$\bar{2}$4}<22$\bar{4}\bar{3}$>	76.89 ° along ($\bar{1}$010)

dislocations on the basal plane [98,99]. The formation of {10$\bar{1}$2} twins by dislocation dissociation mechanism can be summarized as: (1) initial <a> dislocations slip along the basal plane during plastic deformation and then pile-up at the GB [64]; (2) the accumulation of dislocations brings about stress concentration, thereby reducing the critical shear stress and propagating the twin fault [64,98]; (3) initial <a> dislocations dissociated into twinning dislocations and stair rod dislocations, and twinning dislocations glide on {10$\bar{1}$2} twin plane where a nanoscale deformation twin thereby nucleates and grows.

Due to the high shockwave pressure exerted on the Ti alloys during LSP process, deformation twinning with multiple variants could be activated and interact with each other. For example, Huang et al. [51] studied the twin-twin intersection modes and twin distribution of pure Ti after LSP, as shown in Fig. 13. Three twin-twin intersection modes were found: (1) intersection of two {11$\bar{2}$2} twin variants (Fig. 13(b)); (2) intersections between a pair of primary twins (Fig. 13(c–e)); and (3) secondary {10$\bar{1}$2} tension twin intersects with the parent grain (Fig. 13(f)). These twin-twin intersections further subdivided the grains and led to grain refinement. Jia et al. [90] also found a large number of deformation twinning and their interactions in the subsurface layer of the LSPed Ti834 alloys. As mentioned in dislocation evolution part, dislocation density becomes much lower as the shock effect of the LSP treatment decays with increasing depth from the peened surface. Differently, the twin density in the sub-surface area is the highest under 3 LSP impact, than that of other regions, probably due to the balance of stresses and thermal effects [100].

Both impact number and laser energy have a great influence on the response of twins in Ti alloys processed by LSP. Mironov et al. [101] examined the LSP-induced microstructure evolution under different number of impacts. As shown in Fig. 14, the deformation area widened as the number of shocks increased. Only a few {10$\bar{1}$2} twin was found in the three times LSPed sample. With the impact number increased to five, more {10$\bar{1}$2} twins were found (Fig. 14(e)). LSP induced more {10$\bar{1}$2} twin after increasing the impact numbers. Increasing impact numbers or laser intensity can also increase the intersection modes of deformation twins in LSPed pure Ti. Lu et al. [50] studied that a large number of parallel narrow strip micro-twin crystals were found without micro-twin collision under single-impact LSP (Fig. 15(a)). However, when processing pure Ti with three-impact LSP, micro-twins in multiple directions were found in Fig. 15(b), which further collided with each other. Huang et al. [100] investigated the effect of laser intensity on the twin evolution of the Ti17 alloy. As the laser intensity increased, the number of twins increased and collided with each other.

The processing temperature is another factor that significantly affects the formation of twins during LSP. Both WLSP and CLSP are observed to generate more twins compared to LSP at room temperature. For example, Li et al. [67] reported that CLSP treatment on pure Ti resulted in a 133.3% increase in the proportion of the near-surface twin boundaries compared to RT-LSP treatment. Such

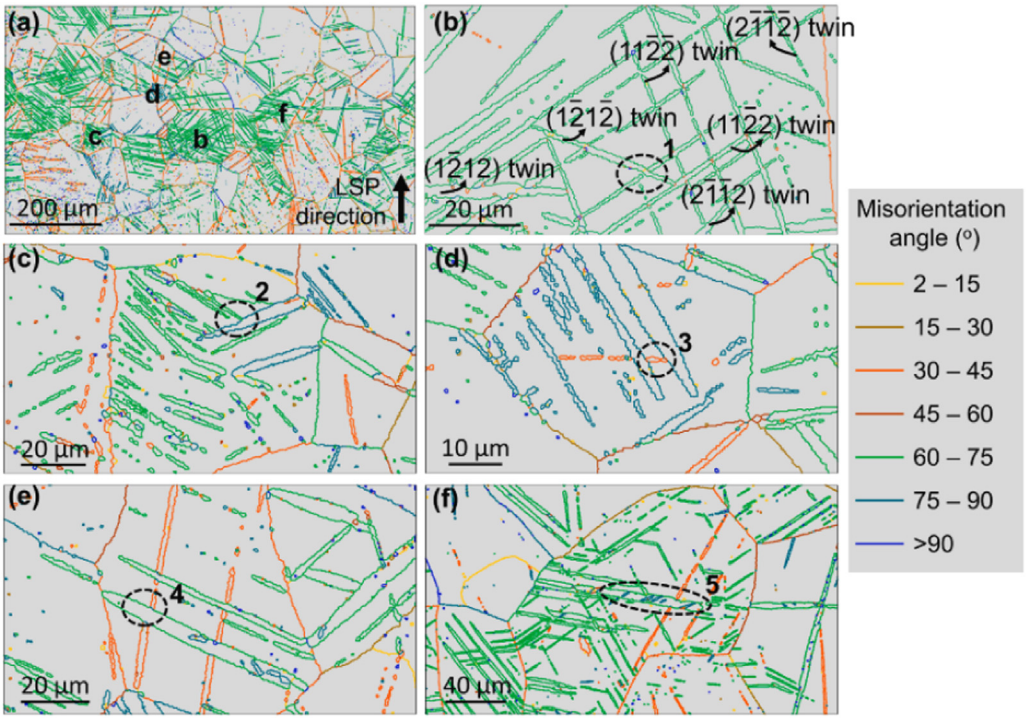

Fig. 13. (a) Microstructure of the pure Ti processed by 3 impacts of LSP. (a) Overview of the microstructure showing the massive twin lamellae. (b-f) Magnified areas in (b) showing the twin-twin intersections. Reproduced from Ref. [51] with permission of the publisher (Elsevier).

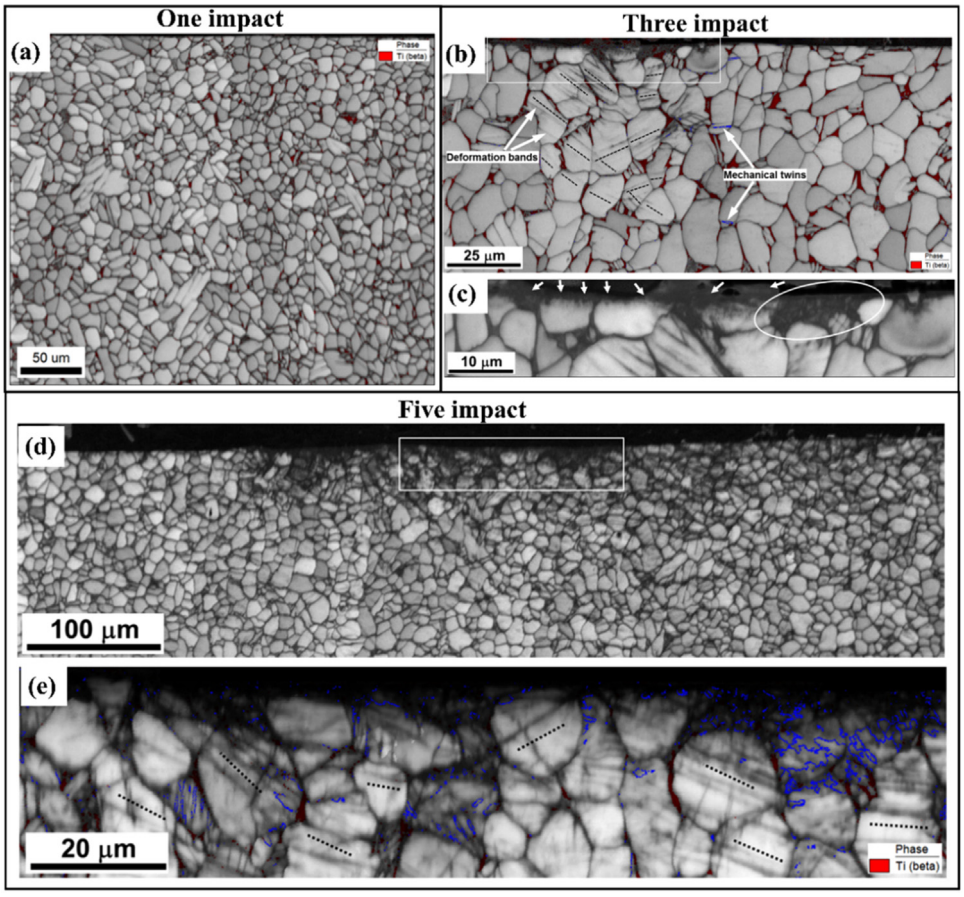

Fig. 14. EBSD image quality map of the cross-sectional microstructure of pure Ti processed by LSP with (a) single impact, (b, c) three impacts and (d, e) five impacts. Reproduced from Ref. [101] with permission of the publisher (MDPI).

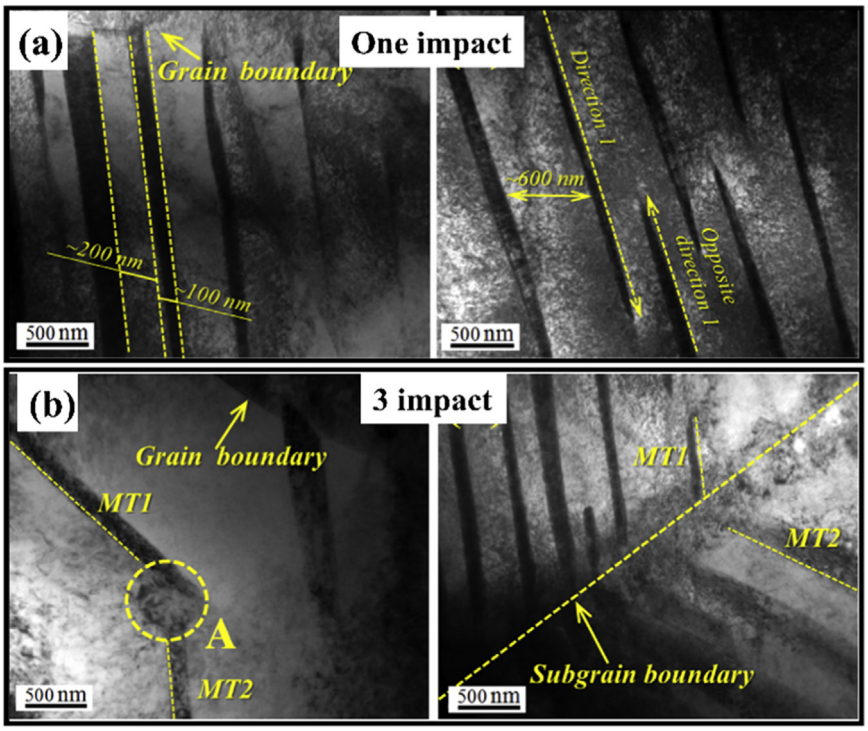

Fig. 15. Typical micro-twin grating in pure Ti subjected to LSP with (a) one impact and (b) three impacts. Reproduced from Ref. [50] with permission of the publisher (Elsevier).

an increase induced by CLSP was attributed to the synergistic effect of cryogenic temperature and ultra-high strain rate plastic deformation. Specifically, the dislocation motion is suppressed under such conditions, thereby elevating the necessity of strain accommodation by deformation twins. In contrast, WLSP, Pan et al. [64] observed a higher occurrence of $\{10\bar{1}2\}$ deformation twins compared to RT-LSP. This was ascribed to the heterogeneous nucleation mechanism: At high temperatures, the improvement in dislocation multiplication (facilitated by the DSA effect) and the enhanced motion of dislocations result in a smoother distribution and densely packed dislocation arrays. This phenomenon provides a rich source of dislocation dissociation in a large-scale. These densely packed dislocations, existing in high-energy states, provide ample driving force for the initial dislocation dissociation and exert strong repulsive forces for the separation of twin dislocations from the core center. In these systems, the nucleation of twins is more favorable, yielding a significant number of $\{10\bar{1}2\}$ twin nuclei.

3.4. Deformation induced phase transformation

Under ambient conditions, the hcp (α) phase of Ti alloys is stable. In 1963, Jamieson reported the pressure-induced $\alpha \rightarrow$ hexagonal (ω) phase transformation in Ti firstly [102]. Therefore, several studies have been carried out to investigate the shock-induced phase transformation in pure Ti [52,84,103]. However, the phase transformation induced by LSP in Ti alloys has rarely been observed, which can be attributed to the high phase transformation energy barrier by the impurity element content [104]. X-ray diffraction (XRD) and selected area electron diffraction (SAED) patterns are widely used to detect the phase transformation of the pure Ti processed by LSP [50,84].

Different LSP parameters affect the formation of ω phase in the pure Ti. Notably, the shock number of LSP has a great influence on the phase transformation of Ti. Li et al. [52] reported the $\alpha \rightarrow \omega \rightarrow$ fcc (β) phase transformations with the increasing shock number in the LSPed ultra-high purity Ti (99.995 %), as shown in Fig. 16(a, b). The first laser shock causes the transition of $\{10\bar{1}0\}_\alpha$ planes to the $\{0002\}_\alpha$ crystal planes, attributing to the $\{10\bar{1}0\}$ planes turn to the vertical axial direction under the high-speed impact pressure. In the second laser shock impact, the $\{0002\}_\alpha$ deformed grains transformed into ω phase at the coherent twin boundaries region when the elastic precursor arrived [105]. Two sets of spots for α and ω phases can be observed in Fig. 16(c). The orientation relationship (OR) of $\{0001\}_\omega$ was paralleled to $\{11\bar{2}0\}_\alpha$, owing to that the $\{\bar{1}\bar{1}20\}_\alpha$, $\{0001\}_\omega$, $\{000\bar{1}\}_\omega$, $\{11\bar{2}0\}_\alpha$ were connected with a line through the central spot. When the number of shocks increases to 3 (Fig. 16(b)), the $\{200\}_\beta$ plane appears, which increases significantly after the fifth impact. The ω phase in the sample is easier to transform to β – Ti than α – Ti, due to the calculated total energies (E) of the phases of titanium in equilibrium volume following $E_\beta > E_{\text{fcc}} > E_\omega > E_\alpha$. With the increase of laser shock numbers, the content of fcc-Ti reaches the maximum, and the impact energy cannot be further consumed through $\alpha \rightarrow \omega \rightarrow \beta$ phase transformations. The different crystal planes of the fcc-Ti were labeled by diffraction spots in the colored circles, as shown in the selective area electron diffraction (SAED) patterns in Fig. 16(d). The intensity of all the diffraction peaks of β – Ti decreases, indicating a $\beta \rightarrow \alpha$ reverse transformation under 8-th shock. Li et al. [84] found the fraction of $\alpha \rightarrow \omega$ phase in pure Ti increased with pulse laser energy, pulse width and the number of impacts.

Except for the occurrence of $\alpha \rightarrow \beta$ phase transformations, the $\beta \rightarrow \alpha$ reverse transformation was found in the LSPed sample with an initial β microstructure accompanied by the martensitic transformation. Lu et al. [50] investigated the martensitic ($\beta \rightarrow \alpha'$) phase transformation of Ti17 alloy processed by LSP. Fig. 17(a, b) displays the typical microstructures of needlelike martensite that were induced by multiple LSP impacts [50]. The formation of hexagonal martensite α' phase facilitated the $\beta \rightarrow \alpha$ reverse transformation (Fig. 17(c)). Under the influence of ultra-strong laser

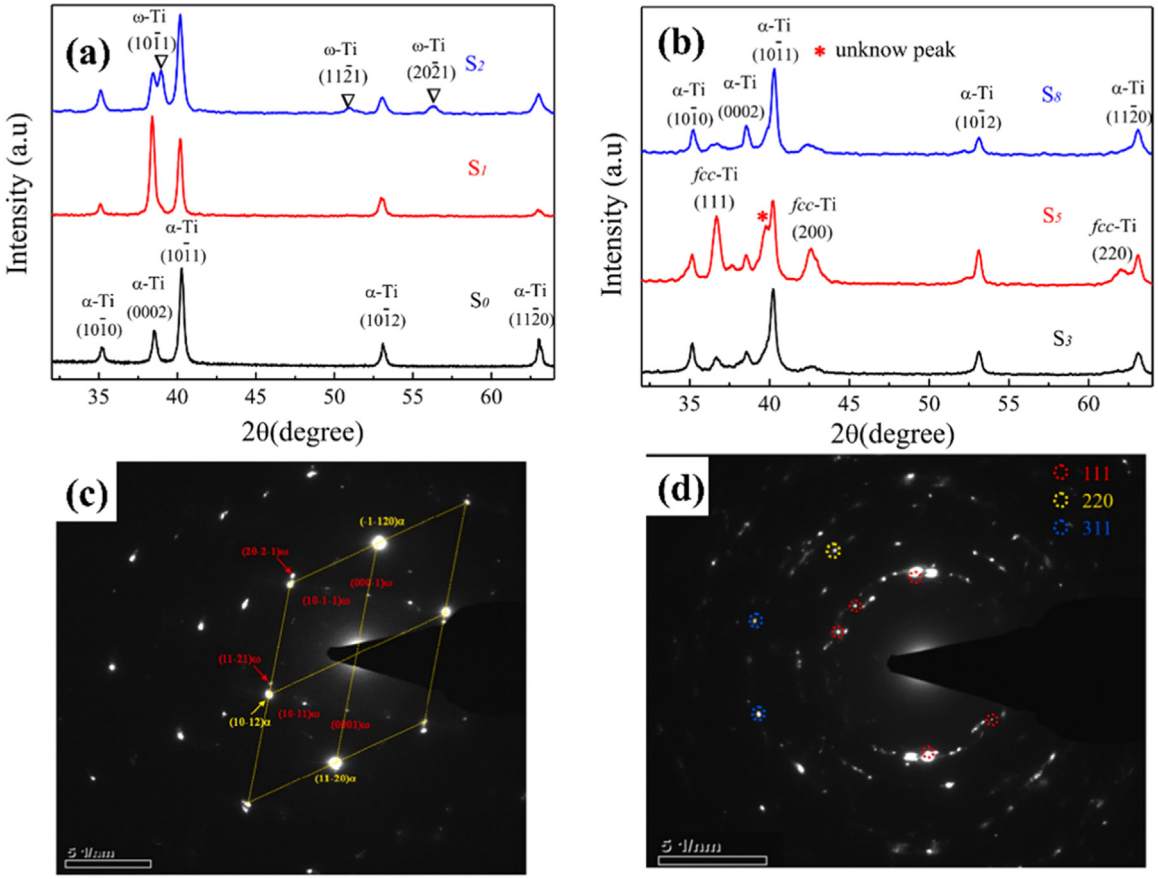

Fig. 16. XRD and SEAD analysis of the pure Ti processed by LSP with different impact numbers: (a, b) XRD analysis, (c, d) SEAD analysis. Reproduced from Ref. [52] with permission of the publisher (Elsevier).

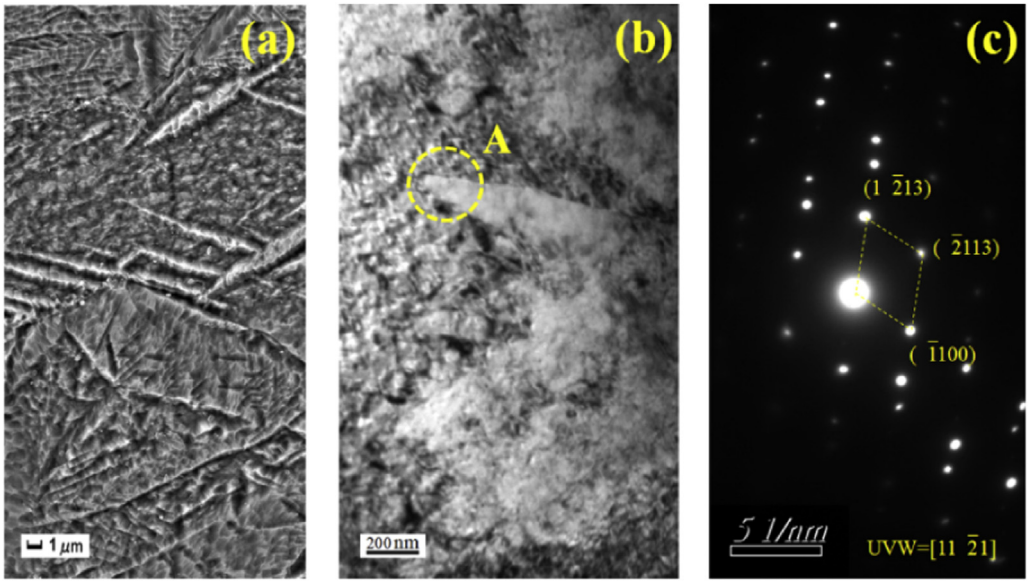

Fig. 17. Typical microstructures of inverse-transformation martensite in Ti17 alloy induced by multiple LSP impacts. (a) Needle-like martensite, (b) TEM micrograph, and (c) the corresponding SAED pattern in circle A. Reproduced from Ref. [50] with permission of the publisher (Elsevier).

shockwave, some trace elements in pure Ti induce lattice distortion and $\alpha' \rightarrow \alpha$ phase transformation, eventually fulfilling the reverse transformation of the $\beta \rightarrow \alpha$ phase. The formation of ω phase was also benefit to the $\beta \rightarrow \alpha$ reverse transformation. Chen et al. [91] found the $\beta \rightarrow \omega$ phase transformation occurred on the bottom surface of Ti17 alloy after two-sided LSP treatment.

3.5. Grain refinement

It has been widely investigated that dislocation accumulation and deformation twinning are the primary microstructural evolution features during LSP of Ti alloys, resulting in significant surface grain refinement [67,83,93,94]. Numerical studies were carried out

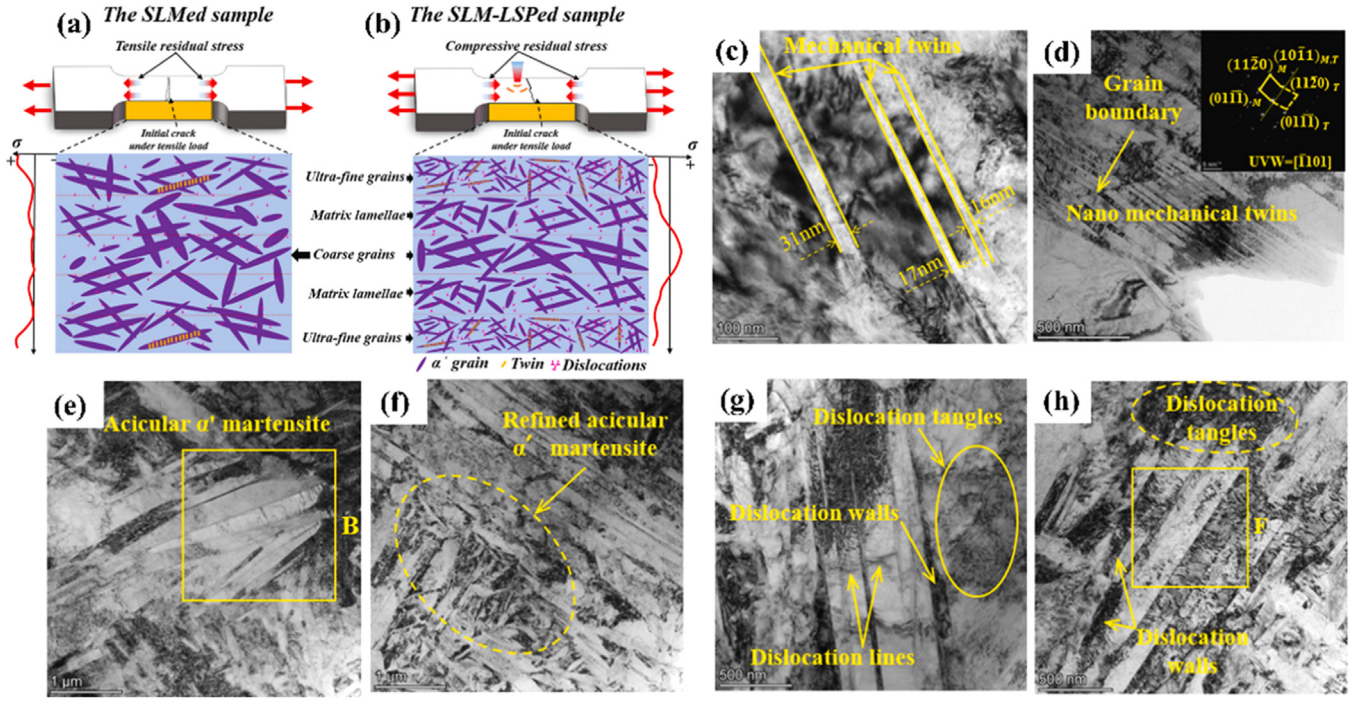

Fig. 18. (a, b) Surface nano-crystallization of Ti64 alloy subjected to LSP impact. Typical TEM images of (c) MTs; (d) nano-MTs; (e) acicular α' martensite; (f) refined acicular α' martensite; (g, h) DTs. The TEM images for (c, e, g) initial sample and (d, f, h) LSPed sample. Reproduced from Ref. [47] with permission of the publisher (Elsevier).

that the surface dislocation cell sizes of pure Ti [83] and Ti64 alloys [95] were refined by the LSP processing. As the laser power density increases, dislocation cell sizes decrease and tend to be saturated. Compared with unLSP-treated Ti alloys, the grain refinement layer induced a higher hardness and then further enhanced the fatigue life by the increased amount of grain boundaries. Detailed analysis of the grain refinement effect was implemented by TEM and IPF maps conducted by EBSD. For example, Zhang et al. [42] showed that the average grain size of Ti64 alloys decreased slightly from 7.7 μm to 6.51 μm after LSP processing. Similar observation was reported by Lv et al. [47] that the average grain width of Ti64 alloys was decreased from 1.51 to 0.95 μm by LSP process on both sides. Additionally, LSP induced a gradient distribution consisting of ultrafine grains at the upper surface, matrix lamellae in the subsurface, and coarse grains in the center area (Fig. 18(a, b)), owing to the attenuation of shock wave in-depth. Three types of grain refinement in selective laser melted Ti64 alloys were found via LSP: (1) grain boundaries induce the segmentation process that from MTs into nano-MT (Fig. 18(c, d)); (2) a large number of parallel MTs with a small number of dislocation motions induce the refinement of α' martensite (Fig. 18(e, f)); (3) DWs (dislocation walls) cut off the long side of α' martensite (Fig. 18(g, h)).

The LSPed grain refinement process for commercial Ti alloys is also affected by the multidirectional interaction of MTs-MTs and MTs-DWs. Lu et al. [50] summarized two subdivision modes that dominated the grain refinement mechanism of LSPed pure Ti, as illustrated in Fig. 19. On the one hand, the multidirectional interaction of MTs-MTs induces grain refinement, including three processes. (1) Parallel MTs with same direction divide coarse grains into thin twin-matrix lamellae (Fig. 19(a, b)). (2) With the increasing impact numbers, various parallel MTs in another direction are introduced into the twin-matrix lamellae, which is further divided into various submicron rhombuses or triangular subgrain blocks (Fig. 19(c)). These subgrain boundaries are arranged in a zigzag shape. (3) After one more LSP impact, parallel MTs in direction 3 causes the elongated lamellae to break laterally (Fig. 19(d)). On the other hand, the interaction of MTs-DWs refines the grain size, which consists of two processes. (1) The formed thin laths (Fig. 19(e)) under one LSP impact are divided by parallel longitude secondary MTs into nanoscale twin-matrix lamellae (Fig. 19(f)). (2) With increasing the strain, the dislocation tends to become arranged in extended DWs, that are approximately perpendicular to the MTs lamellar boundaries, which further separate the nanoscale twin-matrix lamellae into refined blocks (Fig. 19(g, h)).

Besides the intersection models, the grain refinement mechanism is also controlled by the dislocation evolution. Ren et al. [106] studied the dislocation evolution process of Ti64 alloys under different laser energy and impact numbers. Before LSP, the grains of Ti64 alloy had relatively large sizes and some parallel dislocations appeared (Fig. 20(a)). Fig. 20(c, d) shows the dislocation evolution process with increasing impact numbers: low-density dislocations → denser dislocations (or dislocation lines tangle) → DWs → DCs → sub-grain boundaries. The dislocation evolution in the process of laser-induced plastic deformation has been discussed in detail in Section 3.1 [49,107].

Moreover, Tong et al. [85] also found that the variation of the grain size as a function of LSP impact numbers. The average grain size of TC11 alloy at the treated surface of 3, 5 and 7 LSP impacts was inhomogeneous nano-grains, 70–90 nm and 40–60 nm, respectively (Fig. 21). Lu et al. [50] found the average grain size in the top surface layer of the one LSPed pure Ti was approximately 5–7 μm, while that of three LSPed specimens was 3–5 μm.

3.6. Surface amorphization

Amorphization can be considered as an extreme case of grain refinement, where the grains become so small that their boundaries are indistinct. Generally, an amorphous layer is often observed under multiple-shot LSP or LSP with high laser energy [48,49,64,108,109]. For example, a uniform amorphous layer with a depth of 10 nm was identified on the surface of TC6 alloys subjected to five-shot LSP with a laser energy of 6 J (Fig. 22(a)) [86].

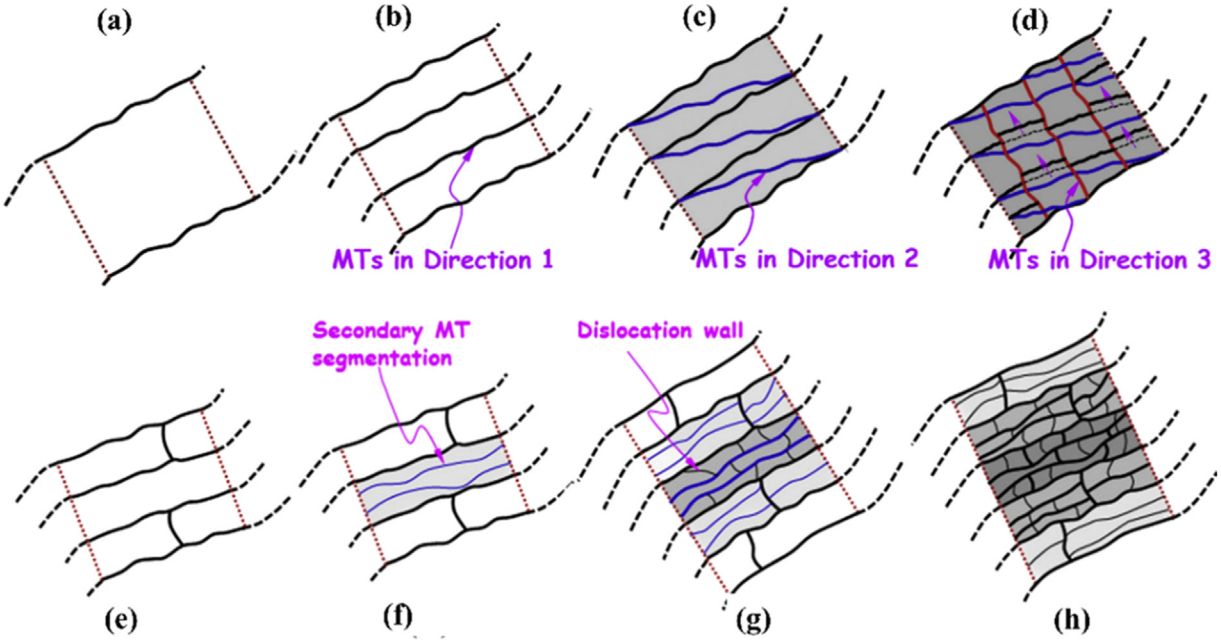

Fig. 19. Schematic representation of (a–d) multi-directional MT-MT intersection process, (e–h) secondary MT-DWs intersections process. Reproduced from Ref. [50] permission of the publisher (Elsevier).

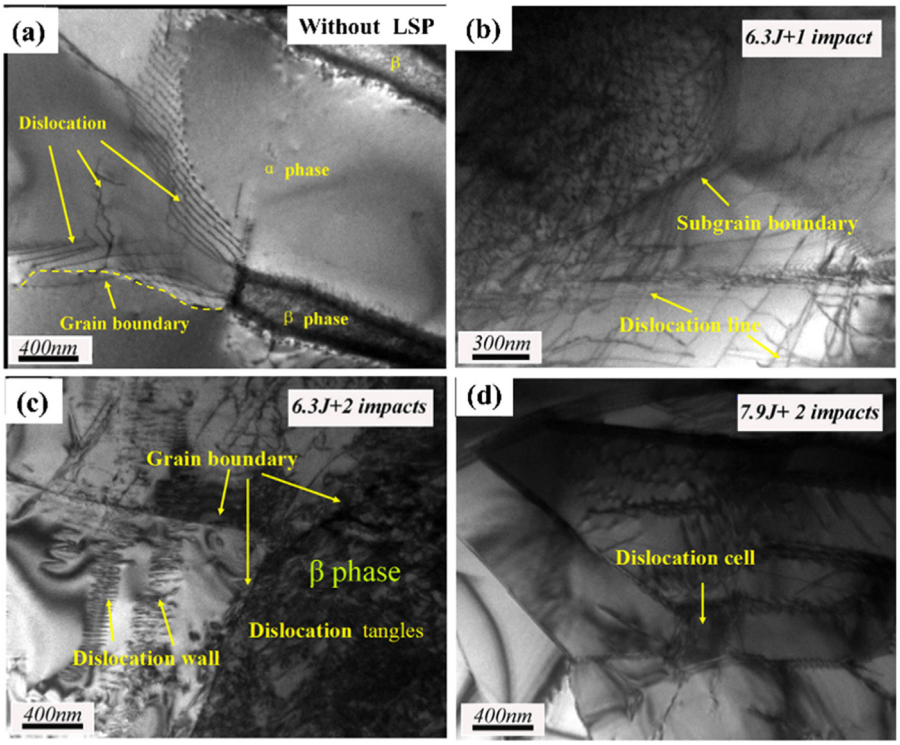

Fig. 20. TEM image of the Ti64 alloys (a) before LSP. Dislocation morphology of Ti64 alloy after LSP with (b) 6.3 J, 1 impact; (c) 6.3 J, 2 impacts, (d) 7.9 J, 2 impacts. Reproduced from Ref. [106] permission of the publisher (Elsevier).

The formation of this layer was attributed to the interactions between numerous dislocations and the high-density stacking faults. A similar phenomenon was reported by Guo et al. [48], where an amorphous layer with a thickness of ~15 nm was observed in a TB10 alloy once the applied laser energy reached 7 J. Such high-energy laser pulse leads to defect accumulation and chemical disorder caused by severe plastic deformation, thereby facilitating the formation of the amorphous layer.

Moreover, researchers have found that high-temperature conditions could promote the surface amorphization of Ti alloys during LSP. In a study by Pan et al. [64], the surface microstructure of Ti64 alloys was examined under LSP and 300 °C-WLSP with the same laser energy of 4 J. An amorphous layer was found on the surface of WLSPed sample, whereas such a layer was absent in the LSPed sample, as shown in Fig. 22(b). This was supported by the TEM analyses that the SAED patterns in the depth direction of the WL-

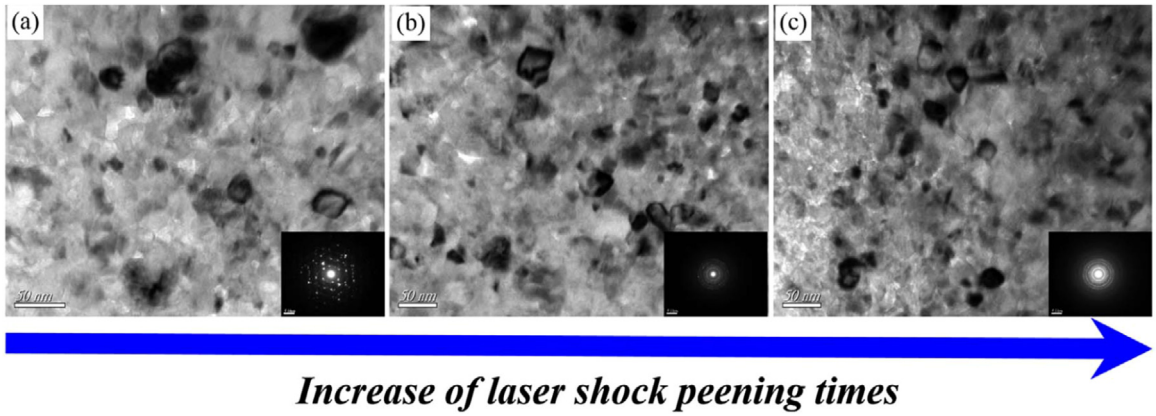

Fig. 21. TEM images of nano-grains at the top surface and the inset showing the corresponding SAED patterns. (a) 3 LSP impacts; (b) 5 LSP impacts; (c) 7 LSP impacts. Reproduced from Ref. [85] with permission of the publisher (Elsevier).

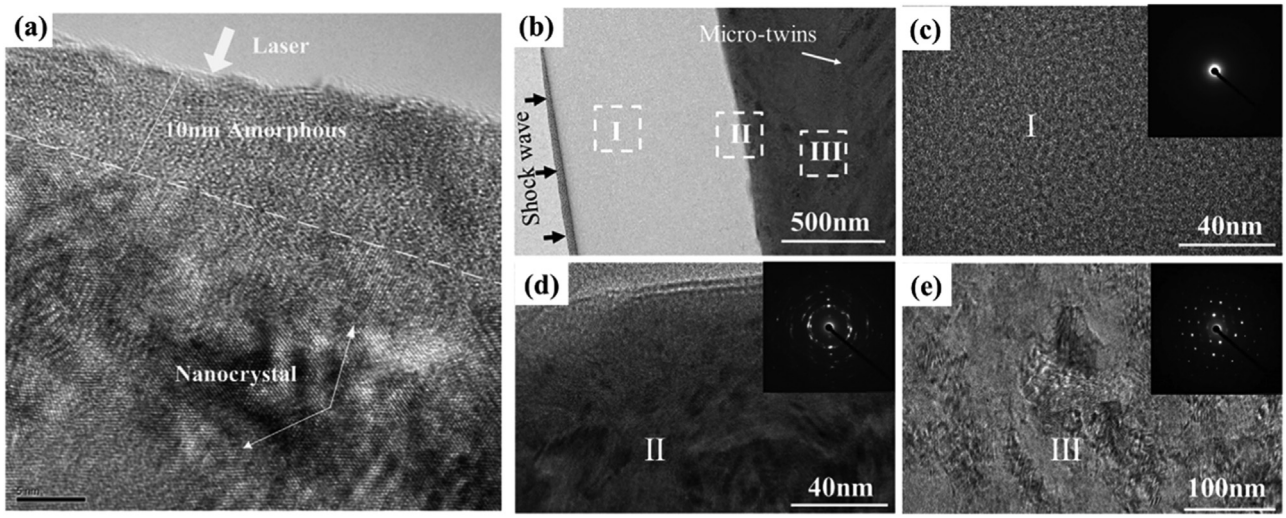

Fig. 22. (a) The microstructure characteristics on the material cross-sectional of TC6 alloy after LSPed [86]. (b–e) Cross-sectional microstructure of Ti64 alloys after WLSP. Reproduced from Ref. [64] with permission of the publisher (Elsevier).

SPed sample transitioned from faint halo rings with no diffraction spots (Fig. 22(c)) to sparse crystalline diffraction spots and uniform rings (Fig. 22(d)), and finally to distinct crystalline diffraction spots (Fig. 22(e)). The facilitation of amorphization layer formation during WLSP was attributed to the increase in free energy arising from the proliferation of dislocations and deformation twins, coupled with a lower energy barrier for crystal-to-amorphous transformation at higher temperatures. Besides Ti alloy that forms an amorphous layer under multiple-shot LSP, LSP with high laser energy and WLSP, the amorphous layer was also identified in H62 brass processed by LSP [108]. However, the effect of the amorphous layer on the engineering performance of LSPed Ti alloys has not been reported so far and deserves further investigation.

4. Enhanced engineering performance

The application of Ti alloys in fields such as aerospace, chemical industry, and medical engineering depends on their properties related to corrosion resistance, wear resistance, and fatigue strength. Therefore, enhancing the engineering performance of titanium alloys (such as CRS, surface hardness, and fatigue life) is crucial during the processing process. In order to improve the engineering performance of Ti alloys, an advanced surface enhancement method known as LSP has been widely used for its excellent surface strengthening effects and deeper CRS layer. Breakthrough investigations of the effect of LSP on engineering performance are catching even more attention. Through LSP treatment, grain refinement significantly enhances surface hardness. The increase in hardness can improve the load-bearing capacity of LSPed titanium alloys, thereby leading to excellent wear resistance. Furthermore, with the advancement of CRS, grain refinement further enhances fatigue fracture resistance, significantly increasing the fatigue limit of Ti and its alloys. LSP-induced grain refinement and crystal defects contribute to the formation of protective mixed oxides, enhancing corrosion resistance. The engineering performance of Ti alloys before and after LSP are compared and summarized in Table 3. These results showed that LSP treatment can significantly improve the engineering performance of Ti and its alloys.

4.1. Introduction of CRS

It is clear that most component failures are caused by external loads or stresses imposed during application. CRS plays a very important role in balancing the external applied stress and therefore improving the engineering performance of Ti alloys. In order to introduce a higher and stabler CRS layer in the Ti alloys, LSP with high energy and ultra-high strain rates are widely used [40,117]. Usually, the LSP-induced CRS field is measured using $\sin^2\psi$-method based on XRD and “Prism” measurement system based on the incremental hole drilling method [45,115,118].

Table 3
Enhanced engineering performance of Ti alloys processed by LSP.

Materials	Power density (GW/cm^2)	Hardness before/after LSP	Max CRS value after LSP (MPa)	Fatigue life before, after LSP (Fatigue strength)	Refs.
Ti834	3.7	330/366 HV	−550	3×10^5, 5×10^5 cycle at 630 MPa	[93]
pure Ti	14.1	171/239 HV	–	–	[50]
pure Ti	6.4	175/330 HV	–	3.6×10^4, 4.7×10^4 cycle at 100 MPa	[110]
Ti64	11.89	319/354 HV	–	600, 700 MPa	[37]
TC6	3.6	6.35/12.86 GPa	−598	–	[70]
TC6	4.24	334.2/409.6 $HV_{0.5}$	−708.5	438.6, 526.7 MPa	[79]
Ti64	3.2/7.2	–	−684/−697	3.48×10^4, 1.81×10^5/3.71×10^5 cycle at 550 MPa	[43]
Ti6Al7Nb	11.5	293/372.2 HV_{30}	–	–	[111]
Ti64	–	361/392 $HV_{0.5}$	−574.9	496.9, 595.4 MPa	[112]
Ti64	5	335 /400 $HV_{0.05}$	−420	216, 306 MPa	[40]
Ti8Al1Mo1V	5.9	–	−570.5	541, 614 MPa	[113]
Ti64	11.3	334/405 HV	−646	51437, 110565 cycles at 540 MPa	[78]
TC11	11.2	362.3/465.7 HV	−598.8	–	[39]
TC11	4.24	351/ 426$HV_{0.5}$	−632.5	483.2, 593.6 MPa	[114]
Ti17	15.92	–	−712	–	[115]
Ti-2.5Cu	5	–	−390	425, 575 MPa	[116]
Ti-54M	5	–	−650	650, 550 MPa	[116]

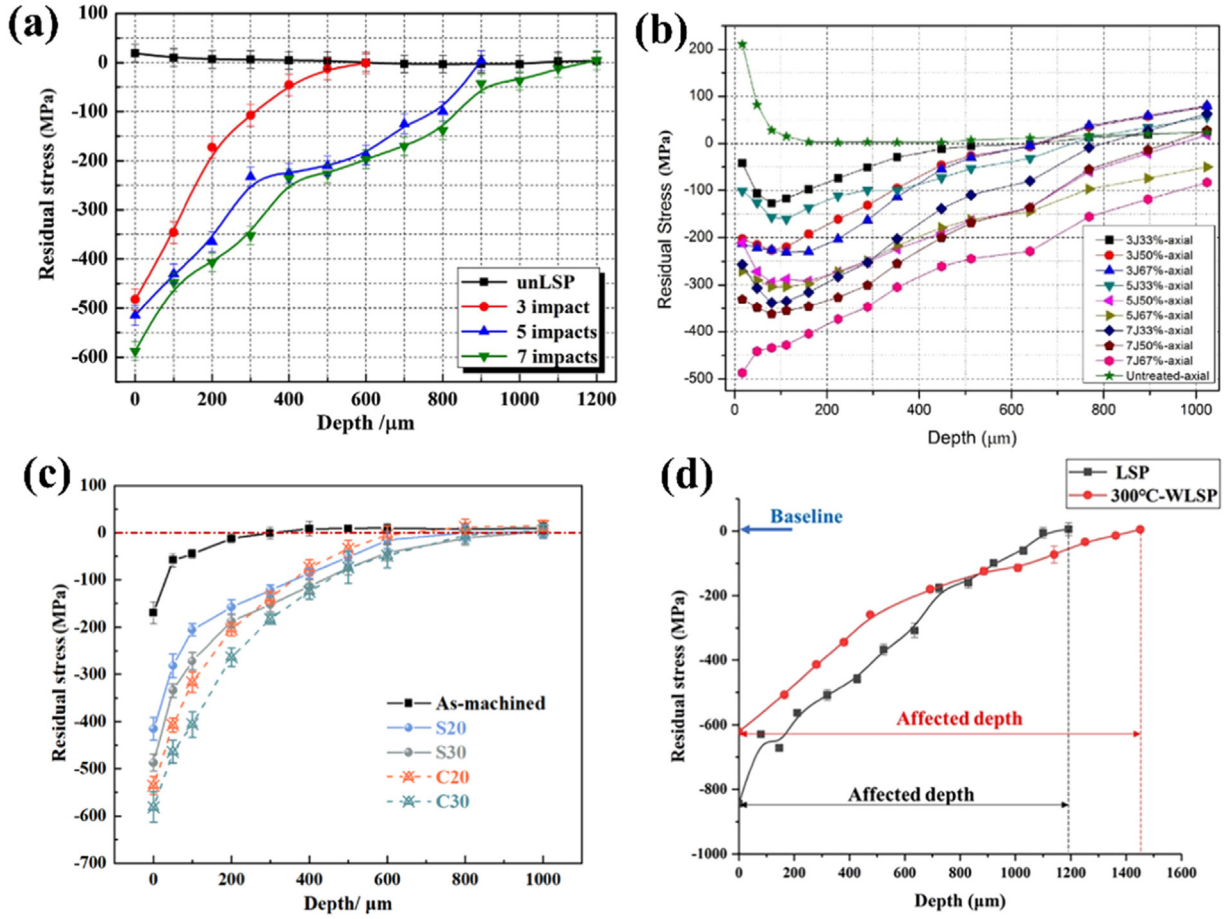

Fig. 23. Variation of CRS introduced in LSP process with (a) the number of shocks, reproduced from Ref. [85] with permission of the publisher (Elsevier); (b) laser energy, reproduced from Ref. [118] with permission of the publisher (Elsevier); (c) laser spot geometries, reproduced from Ref. [45] with permission of the publisher (Elsevier); (d) WLSP, reproduced from Ref. [64] with permission of the publisher (Elsevier).

The LSP-induced CRS value of Ti alloys is affected by some LSP process parameters: laser energy, impact number, and overlapping ratio. For example, Tong et al. [85] found that the increasing LSP impact numbers can effectively increase the depth of CRS in TC11 Ti alloy (Fig. 23(a)). The same phenomenon was reported in near-α Ti alloy [93] and Ti64 alloy [40,87,93]. Notably, Maawad et al. [116] mentioned that the surface residual stresses of Ti alloy were compressive after 16 hits under the smaller pulse energy (0.05 J) of LPwC. However, Cellard et al. [119] supported that the influence of the number of impacts is moderate. One impact is enough to bring the Ti17 alloys to saturation, resulting in a drop in the CRS. Compared to the relatively minor effect of LSP impact numbers on CRS, both increasing the laser energy and the overlapping ratio could significantly increase the magnitude of the surface CRS

and the overall depth of the CRS. Shen et al. [118] found the near-surface CRS values of Ti6Al7Nb that treated by 3, 5, and 7 J were −42, −101, and −257 MPa, respectively (at the 33% overlay). With the overlapping ratio increased to 50% (67%), the near-surface CRS values of Ti6Al7Nb that were treated by 3, 5, and 7 J increased to −212 MPa (−234 MPa), −261 MPa (−297 MPa), and −331 MPa (−516 MPa), respectively (Fig. 23(b)). Compared with the tensile stress of 225 MPa in the top surface of untreated Ti6Al7Nb, the magnitude of CRS of LSPed sample increased obviously.

Additionally, the CRS value of LSPed region can be affected by LSP process strategies, such as laser scanning direction and spot geometry. For instance, Zhang et al. [45] compared the effects of square and circular spots on the CRS of Ti64 alloys. It was reported that the maximum values of CRS for as-machined, square spot and circular spot were −170, −415 and −535 MPa, respectively. Both the circular spot and square spot induce higher CR than that of as-machined sample, while the circular spot has the highest CRS (Fig. 23(c)). The different scanning directions of the laser beam also have a great influence on the CRS. Jia et al. [93] and Maawad et al. [116] found the CRS of Ti834 alloy and Ti-2.5Cu alloys in *y* direction was larger than that in *x* direction after LSP.

Temperature is an important parameter that influences the distribution of CRS. Pan et al. [64] studied the effect of temperature on CRS distribution of Ti64 using WLSP. The results showed that the surface CRS of LSPed and WLSPed Ti64 alloys was significantly above the initial sample (-250 MPa). The CRS layer in the WLSPed sample was 21.8% higher (1.45 mm) than in the LSPed sample (1.19 mm), which was attributed to the dynamic strain aging (Fig. 23(d)). Zhou et al. [65] showed the amplitude of CRS in LSPed Ti64 alloys increased gradually with increasing temperature from 20 to 100 °C, whereas decreased sharply once the temperature exceeded 100 °C.

4.2. Enhanced surface hardness and wear resistance

Hardness is among the most important engineering properties of a material, as it represents the local deformation resistance of materials. Therefore, understanding the hardness variations can be preferred to assessing the quality of LSP on Ti alloys. Vickers hardness testing was used to evaluate the hardness evolution after LSP. It is well known that the increased surface microhardness by LSP is mainly ascribed to the synergy effect of increased grain boundary area and dislocation density.

According to the Hall-Petch effect [47,51], the improved hardness due to grain refinement can be described by:

$$\sigma = \sigma_0 + kd^{-\frac{1}{2}} \tag{8}$$

where k is a measure of the local stress needed to initiate plastic flow at a grain boundary, σ_0 is the resistance to dislocation motion in the grain interior, and d is the grain size. After LSP, the grain refinement process of Ti alloys is controlled by dislocations, twins and their interactions, leading to a higher hardness than that for the untreated sample [106].

The dislocation strengthening contribution can be predicted by the Taylor hardening:

$$\sigma = M\alpha Gb\sqrt{\rho} \tag{9}$$

where M is the Taylor factor (for HCP metals, $M = 2.8$), α is a constant of 0.20 [120], G is the shear modulus of 44 GPa [121], and b is the magnitude of the Burgers vector. ρ is the dislocation density, which is obtained from the XRD calculations.

LSP induced the gradient microhardness distribution, which was increased to different levels at different depths due to the evolution of dislocations and grain boundaries. As shown in Fig. 24(a), the strengthening behavior was divided into four stages: stage I: formation of dislocation lines and dislocation arrays; stage II: formation of dislocation tangles and dislocation walls; stage III: formation of dislocation cells, and stage IV: formation of mechanical twins and sub-grains. As the depth increased, the role of the dislocation gradually decreased. Moreover, according to the estimated microhardness by synergistic strengthening (Fig. 24(b)), the effects of both dislocations and grain boundaries were decreased with the increasing depth. The contribution of dislocation strengthening was much greater than that of grain boundary strengthening at the surface [42,51].

Both increasing the laser energy and the impact number could increase the surface hardness. Ren et al. [106] studied the effect of laser energy and impact number on the surface hardness of LSPed Ti64 alloys. As shown in Fig. 25(a), under a single impact, the surface hardness of untreated, 6.3 and 7.9 J was 330, 390 and 415 HV, respectively. With the rising of impact number (2 impacts), the surface hardness of 6.3J and 7.9J was increased to 412 and 430 HV, respectively. With the increase of laser energy and impact number, the surface hardness was improved due to the generation of more dislocation obstacles. A similar phenomenon was observed by Lu et al. [50] and Nie et al [114].

Temperature is also an important parameter to affect the surface microhardness (Fig. 25(b, c)). As shown in Fig. 25(b), Pan et al. [64] found that the average surface microhardness of LSP and WLSP were 15.4% and 20.8% higher than the baseline value (331 HV). At the same depth, the WLSPed Ti64 alloys were harder than their LSPed counterparts. The surface microhardness improvement after WLSP was attributed to the denser dislocations and numerous deformation twins than those for LSP. Although a 10 nm

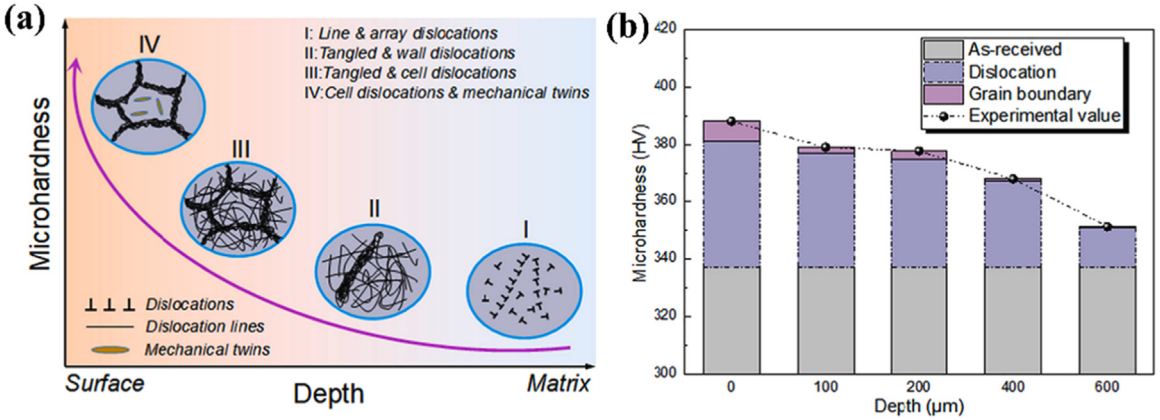

Fig. 24. (a) Schematic of the relationship between microhardness and microstructures. (b) Estimated microhardness by synergistic strengthening. Reproduced from Ref. [42] with permission of the publisher (Elsevier).

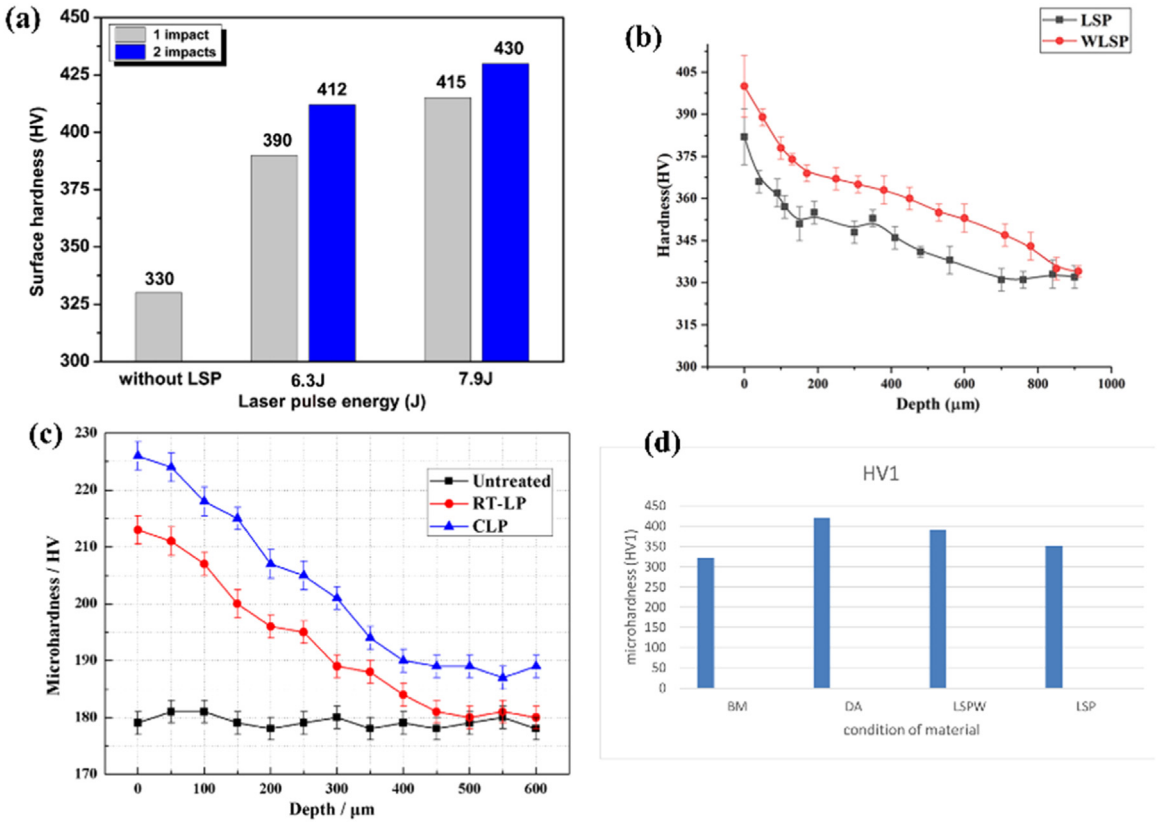

Fig. 25. (a) Surface hardness of Ti64 alloy before and after LSP, reproduced from Ref. [106] with permission of the publisher (Elsevier). (b) In-depth hardness distributions in Ti64 alloys treated by LSP and WLSP, reproduced from Ref. [64] with permission of the publisher (Elsevier). (c) In-depth microhardness distribution of the pure Ti after different treatments, reproduced from Ref. [67] with permission of the publisher (Elsevier). (d) Microhardness values of LSPed Ti64 alloys depending on the condition of protective coating layer, reproduced from Ref. [122] with permission of the publisher (Elsevier).

amorphous layer was introduced by WLSP, its influence on the surface hardness has not been mentioned. Such an enhanced surface-hardening phenomenon has been also reported in cryogenic treatment. Li et al. [67] showed that the surface microhardness of the CLSPed pure Ti (226 HV) was 6.1% and 23.8% higher than that of untreated sample (180 HV) and LSPed sample (213 HV), respectively (Fig. 25(c)).

In addition to the laser processing parameters, the protective coating also affects the enhanced surface hardness. Protective coating is generally used to protect the substrate from the thermal effect induced by laser-matter interaction [24]. By comparing the effects of LSP and LPwC on Ti alloy, Petronić et al. [122] showed that the microhardness of Ti64 alloys under LSP without a protective and transparent layer was higher than that of LPwC, while that of LSP was the lowest (Fig. 25(d)). With or without the coating layer, the LSP can increase the surface hardness of Ti64 alloys. The mechanisms of hardness increasement under LPwC on Ti64 alloys was attributed to the formation of alpha layer [123] and grain refinement [124].

The increment in hardness could enhance the load-bearing capacity of the LSPed Ti alloy, which brings in a good property of wear resistance. The friction and wear tests were performed on the Pin-on-Disk tribometer under dry sliding conditions. An Al_2O_3 ceramic ball or hardened steel ball was employed as the counter ball [39,111]. Shen et al. [111] found that after 3 multiple LSP impacts, the microhardness of Ti6Al7Nb alloys presented an improvement of 22.31% than untreated sample (300 HV_{30}), leading to the sliding wear of samples improved by 44%.

The LSP-enhanced wear resistance is influenced by the laser parameters, such as impact number and laser energy. As shown in Fig. 26(a), the friction coefficient of impacted Ti6Al7Nb decreased with shock impact numbers. Fig. 26(b) showed the wear mass loss of impacted samples was 1.6 × 10^{-5}, 15 × 10^{-5}, and 12 × 10^{-5} g for 1, 2, and 3 impact numbers, respectively. Through the SEM observation, the track of impacted surfaces was much smoother than as-received samples (Fig. 26(c, d)). The wear mass loss was decreased with the impact numbers. The results indicated that with the increase of impact numbers, the sliding wear performance of Ti6Al7Nb improved, which was related to the decrease in grain size and the increase in surface hardness. Varying the laser energy of LSP has a great effect on the wear resistance of Ti alloys. Yin et al. [125] found the wear scars of the untreated, 5 and 7 J were 355.7, 318.7, and 280.1 μm, indicating that the LSPed Ti64 alloy had superior wear properties than that of as-received specimen. The improving wear resistance after LSP was attributed to the increased surface hardness and CRS.

To further study the effect of LSP impacts, Tong et al. [39] studied the sliding friction and wear properties of untreated and LSPed Ti alloys under temperature and applied load. Fig. 27(a) showed the wear rates of untreated and LSPed TC11 alloy decreased from 25 to 500 °C, and increased with the test temperature increasing to 600 °C. As compared with the untreated specimen, the wear rate all decreased after LSP impacts at different temperatures. At 25 °C, the smearing, adhering and deep grooves was found in the sliding wear contact surfaces of untreated and LSP (Fig. 27(b, c)). The rapidly increased temperature on the worn surface contributed to the formation of black smooth regions (oxidation layers), as shown in Fig. 27(d–f). It proved that the predominant wear mechanisms at 25 °C were adhesive and abrasive wear. With the temperature increased to 400, 500 and 600 °C, the main wear mechanisms were abrasive wear, generation and breakdown of oxidation films. The lowest wear rate was obtained for the LSPed specimen un-

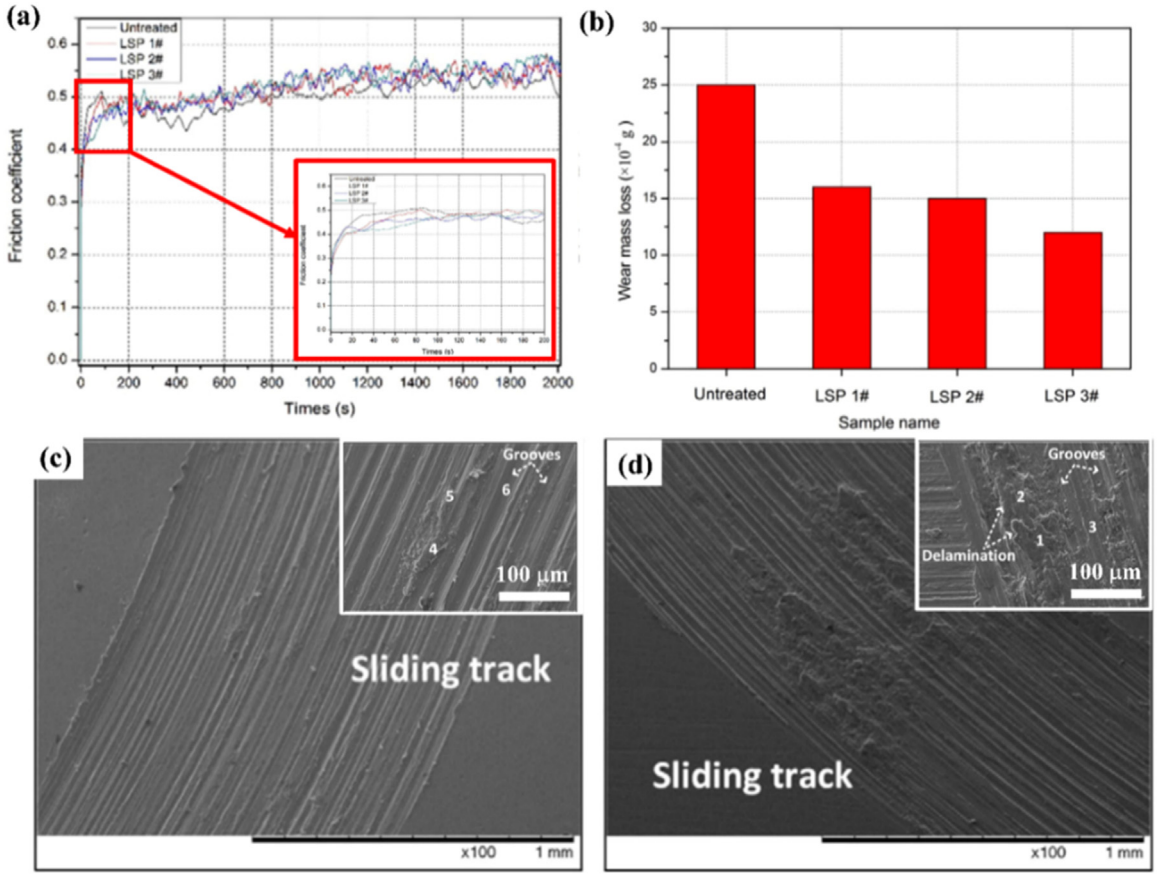

Fig. 26. (a) Friction coefficients of different impacts of Ti-6Al-7Nb alloy vary with time: 0 s to 2000 s. (b) Wear mass loss of Ti-6Al-7Nb alloy with and without LSP processing. SEM images of the worn surfaces of the sample (c) without and (d) with 3 impacts LSP processing. Reproduced from Ref. [111] with permission of the publisher (Elsevier).

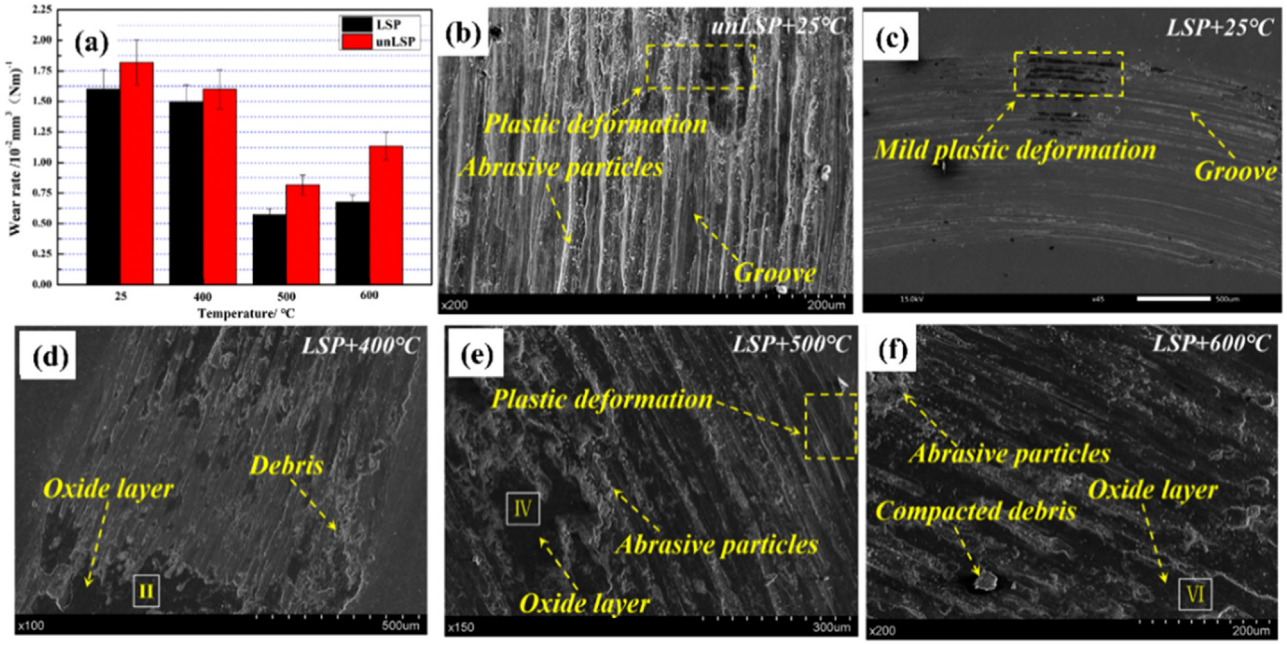

Fig. 27. (a) Wear rates of specimens at different temperatures under a normal loading of 15 N. SEM images of the worn surfaces for (b) untreated at 25 °C, LSPed specimens at (c) 25 °C, (d) 400 °C, (e) 500 °C, (f) 600 °C. Reproduced from Ref. [39] with permission of the publisher (Elsevier).

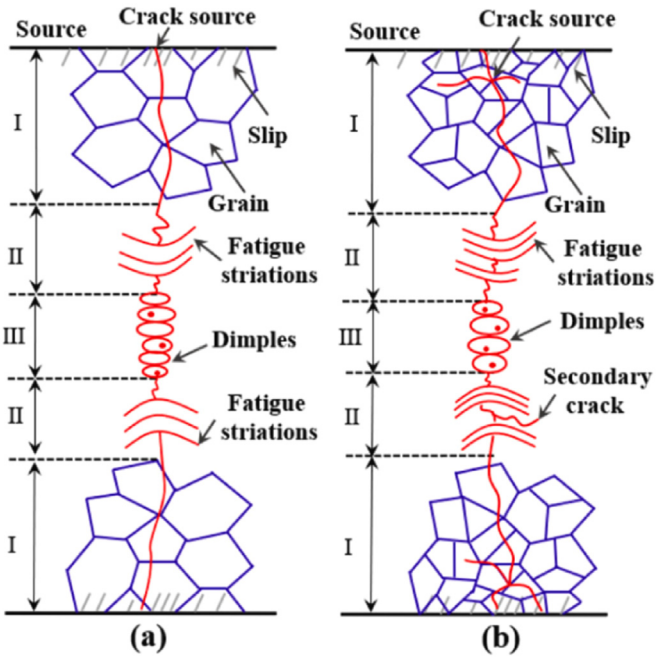

Fig. 28. The mechanism of improved fatigue durability of Ti alloys processed by LSP. Crack propagation in Ti alloy (a) without and (b) with LSP processing. Reproduced from Ref. [70] with permission of the publisher (Elsevier).

der the applied load of 15 N at 500 °C, due to the formation of dense oxidized titanium and aluminum film. Obviously, the wear rate of the LSPed specimens was increased with the applied load from 10 to 15 N. Under the same wear condition, all the wear rates for the LSPed specimens were lower than that of untreated specimens. The enhanced tribological properties of the LSPed specimen were attributed to the effective retardation of crack nucleation and growth during the wear process, owing to work hardening, CRS, and grain refinement.

4.3. Enhanced fatigue life and strength

When Ti-based components are subjected to external loads, stress concentration sites in components can facilitate crack initiation and propagation, ultimately reducing the fatigue life. Fatigue durability tests were performed using a fatigue machine with test specimens mounted in axial compression-tension or three-point/four-point bend configuration [36,43,126]. The typical fracture morphologies of fatigue specimens are shown in Fig. 28(a), which is mainly composed of fatigue crack initiation (FCI) I, crack propagation area II and final fracture area III. As shown in Fig. 28(b), the concurrent development of CRS and grain refinement through LSP significantly enhances the resistance to fatigue fracture, as evidenced by the notable improvement in the fatigue limit of Ti and its alloys [79,114,115]. The grain refinement layer generated via LSP creates a barrier, limiting the growth of cracks through the increased grain boundaries [37]. It is worth noting that the high magnitude CRS induced by LSP plays a dominant role in suppressing the initiation and propagation of cracks by reducing the effective mean stress during cyclic loading [44,126]. The beneficial effect of CRS layer on enhancement of the fatigue performance is concluded as follows:

(1) LSP-induced CRS can counteract a part of work tensile stress and enhance the fatigue limit of the strengthened layer. Consequently, in the fatigue crack initiation stage (area I in Fig. 28(b)), CRS compels fatigue cracks to initiate at the vulnerable area, where with much smaller working stress and more restrictions for deformation than that at the surface; (2) LSP-induced CRS can decrease stress intensity factor range ΔK and stress ratio R and increase of closing force of microscopic crack [127]. Therefore, in the growth stage of fatigue crack (area II in Fig. 28(b)), CRS can improve the threshold of crack growth and retard crack propagation [114].

The fatigue lives of LSPed Ti alloys are influenced by key factors, such as laser power density [115] and impact number [40]. Wang et al. [36] studied the effect of laser energy and impact numbers on the fatigue properties of LSPed Ti64 alloys. Usually, S–N curve has been expressed in the form of an exponential relationship between applied stress σ and number of cycles to failure, presenting the mechanistic view of the fatigue phenomena [128]. From the fatigue S–N curves of (Fig. 29(a)), the crack origin zone shifts sideways, which reflects the fatigue-strengthening effect of LSP on the selected region of initial Ti64 alloys. Under high-cycle fatigue (HCF) regime, with the increase of laser energy and impact numbers, the fatigue strengthening effect was similar [43,45,90,115]. However, the fatigue strength in ultra-HCF region deteriorated after 4.6 J impact for 3 times. The result showed that only the ultra-HCF properties were related to impact parameters. In addition, Jiang et al. [129] showed the S–N curves continued to decline in the ultra-HCF region regime after LSP (Fig. 29(b)), and disparity of fatigue strength between heat-treatment and LSP became larger. The deterioration of fatigue strength for multiple LSPed Ti alloys during ultra-HCF region was attributed to two reasons: (1) the increased surface roughness under multiple shock induces surface damage (micro notches); (2) a tensile stress core in the midsection and inherent defects of the LSPed specimens leads to a higher crack growth rate.

LSP process strategies are important factors to be considered, such as laser spot geometries and protective coating. Zhang et al. [45] reported the effect of spot geometries on fatigue life of LSPed Ti6Al4V alloys. The results showed that the fatigue life of LSPed sample with square spot (89518 cycles) and circular spot (126709 cycles) was 1.68 and 2.38 times that of the unpeened samples (53252 cycles), respectively. The results showed that circular spot has a more prominent strengthening effect on the fatigue life of LSPed Ti6Al4V alloys than square spot, possibly due to the more homogenous microstructure modification induced. Besides CLSP treatment, the effect of LPwC on the fatigue life of Ti alloys is still controversial. Pan et al. [130] investigated that the fatigue limits of unpeened Ti64 alloy were 16% lower than LPwCed samples, which increased from 264 MPa to 305 MPa. In contrast, Maharjan et al. [123] found that LPwC does not contribute to the improvement of the fatigue life of Ti64 alloys, owing to the formation of the brittle alpha layer in the surface and the introduction of tensile residual stress. Praveenkumar et al. [131] reported that there was an oxide layer (TiO) had formed on the surface of the LPwC Ti64 alloys, instead of brittle alpha. The oxide layer induced by LPwC introduced a tensile residual stress of 65 MPa.

In addition to adjusting process strategies of LSP, temperature has a significant effect on the fatigue performance of the Ti alloy. For example, the CLSP treatment can significantly enhance the high-cycle bending fatigue of TC6 alloy. Li et al. [70] found that the damping ratio of the CLSPed with 143 K TC6 alloy increased by 15.4% than that of the LSPed TC6 alloy. Compared with the untreated (8.86×10^5 cycles) and RT-LSP (12.69×10^5 cycles) specimens, the fatigue life of the specimens treated by CLSPed with 143 K reached 16.87×10^5 cycles, which increased by 90.41% and 32.94%, respectively. The deformation twin induced by CLSP can reduce the stress concentration on the surface, thereby effectively suppressing the cracks initiation.

LSP can significantly enhance the fatigue life of Ti alloys with different shapes. For example, Sun et al. [132] studied the effect of hole drilled prior and post to LSP on the fatigue of Ti17 alloy, which indicates that drilling after LSP is an optimal process-

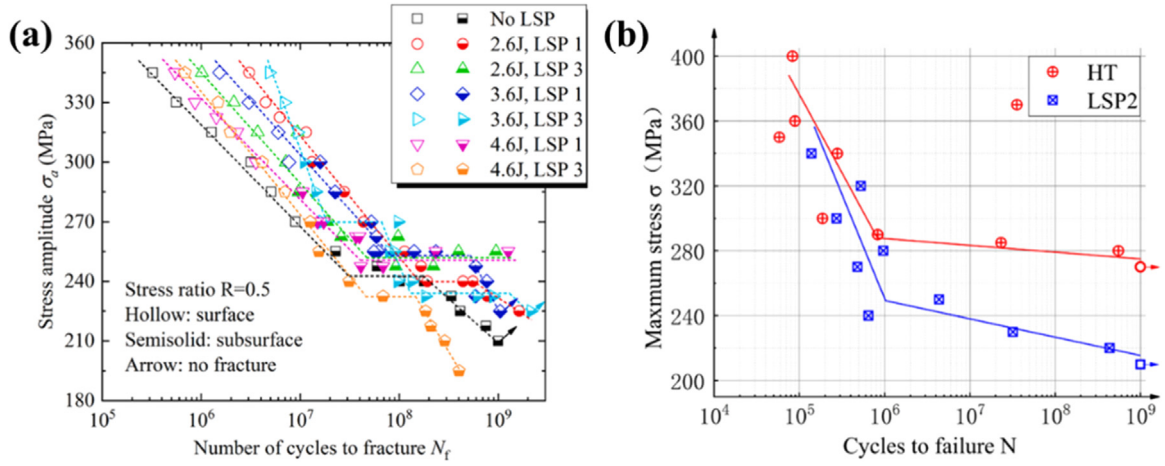

Fig. 29. (a) S–N curves of the LSP processed Ti alloys with different processing parameters, reproduced from Ref. [36] with permission of the publisher (Elsevier). (b) S-N curves of the tested Ti64 alloys, reproduced from Ref. [129] with permission of the publisher (Elsevier).

ing procedure (significantly increased by 330% than non-drilled sample). Two-sided and simultaneous LSP (TSLSP) experimental results showed that maximum fatigue life increases by 94% (directly TSLSP) and 169% (TSLSP with 2 mm away from the leading edge) compared with the original Ti64 [44].

In the actual service conditions of these aerospace engine components, Ti alloys were subjected to the combined effects of temperature cycling and applied mechanical stresses. As the coupling of LCF and thermal fatigue, thermomechanical fatigue properties are a reliable predictor of actual operating conditions. Wang et al. [78] investigated the thermomechanical fatigue properties of Ti64 alloys under LSP. Compared to the untreated Ti64 alloys, the thermomechanical fatigue lives of the LSPed specimens with one coverage layer and two coverage layers increased by 48.00 % and 114.95 %, respectively. Under a high temperature of the heat cycle, the fatigue life of the LSPed specimens with two coverage layers was increased by 68.91% even. In the thermal fatigue test, the LSP-induced CRS, high-density dislocations and refined grains make a significant contribution to the inhibition of microcrack initiation and growth.

Furthermore, dimensions of the LSPed regions play an important role in the fatigue life of Ti17 alloy (Fig. 30). Sun et al. [60] found that the fatigue life increased by 38% and 50% with Type-I and Type-II peened regions, while it decreased by 13% when employing Type-III peened region. The main factor is the discontinuity on the edge due to the interaction between the shock wave and the specimen edge. As shown in Fig. 30(a0–a3), the FCI sites of the original and Type-III specimens were located on the top surface of the specimen, while that of Type-I and Type-II were located on the side surface. The FCI sites were transited from surface to subsurface, implying a delay of cracks initiation and a prolongation of fatigue lives. The same transition process was found in the LSP and CLSP treated TC6 alloys [70]. By comparing the propagation zone of different types (Fig. 30(b0–b3)), the averaged striation width of Type-I and Type-II was smaller than the original and Type-III specimens. Fig. 30(c0–c3) shows the Type-I and Type-II specimens have more small voids and equiaxial dimples than the initial and Type-III specimens, which indicates that LSP can postpone the generation and propagation of the crack, thus increasing the fatigue performance.

4.4. Enhanced corrosion resistance

Owing to excellent engineering properties (high strength and low Young's modulus), and excellent biocompatibility, Ti alloys have been extensively applied in the biomedical implant market and the aerospace industry [133,134]. Ti alloys are sustained by the influence of the surrounding media (acids, alkalis, and salts, etc.), as well as high temperatures. This would significantly decrease the engineering performances of Ti alloys, and shorten the service life of the equipment. In order to enhance the corrosion resistance of Ti alloys, LSP has already been successfully applied to various Ti alloys and proved its ability to improve the corrosion resistance of Ti alloys. Ti alloys were typically exposed to the molten salt atmosphere and air at high temperatures to evaluate the hot corrosion [135,136]. Isothermal oxidation tests were conducted in a timer-controlled resistance furnace under static air [137,138]. The initial and final weights of the Ti alloys were measured to assess the mass gains. Electrochemical experiments were carried out with a three-electrode cell system to obtain the polarization curve [137].

The LSP-induced grain boundary effect and the superior plastic deformation can improve hot corrosion resistance of Ti alloys. Geng et al. [136] used LSP to enhance the hot corrosion resistance of TC21 alloy. Compared with the untreated specimens, the mass gains of LSPed TC21 alloy after hot corrosion at 700 and 800 °C were decreased from 5.65 and 6.81 mg/cm^2 to 3.72 and 4.78 mg/cm^2, respectively. The enhanced hot corrosion resistance after LSP was attributed to that crystal defects can increase the diffusion channels of elements, thereby assisting the formation of protective mixed oxides and improving the adhesion between the outer oxide layer and the substrate. Lu et al. [135] also found that LSPed Ti64 had lower mass gain after hot corrosion compared with the initial specimen, especially at 700 °C.

LSP can also effectively improve the oxidation resistance of Ti64 alloy produced by laser additive manufacture. Guo et al. [138] studied the effects of LSP treatment on the high-temperature oxidation resistance of NiTi alloy. As shown in Fig. 31(a), the oxidation weight gain per unit surface area of LSP-treated sample was lower than that of untreated samples at the same temperatures. In Fig. 31(b), the activation energies of the LSPed samples in the 400–800 °C were increased by 10.3% than untreated samples, indicating the enhancing antioxidant properties. The increasing oxidation resistance of the Ti64 alloy after LSP was attributed to the reduction of oxide particle size on the surface (Fig. 31(c)). Moreover, compared with one Al-rich zone in untreated samples, LSP induced the formation of three Al-rich zones (Fig. 31(d, e)). The multiple Al-rich zones facilitated the formation of a dense Al_2O_3 layer, further preventing oxygen from diffusing into the substrate.

Ti alloys can be adjusted to obtain different microstructures with different plastic deformability, each of which has a distinct

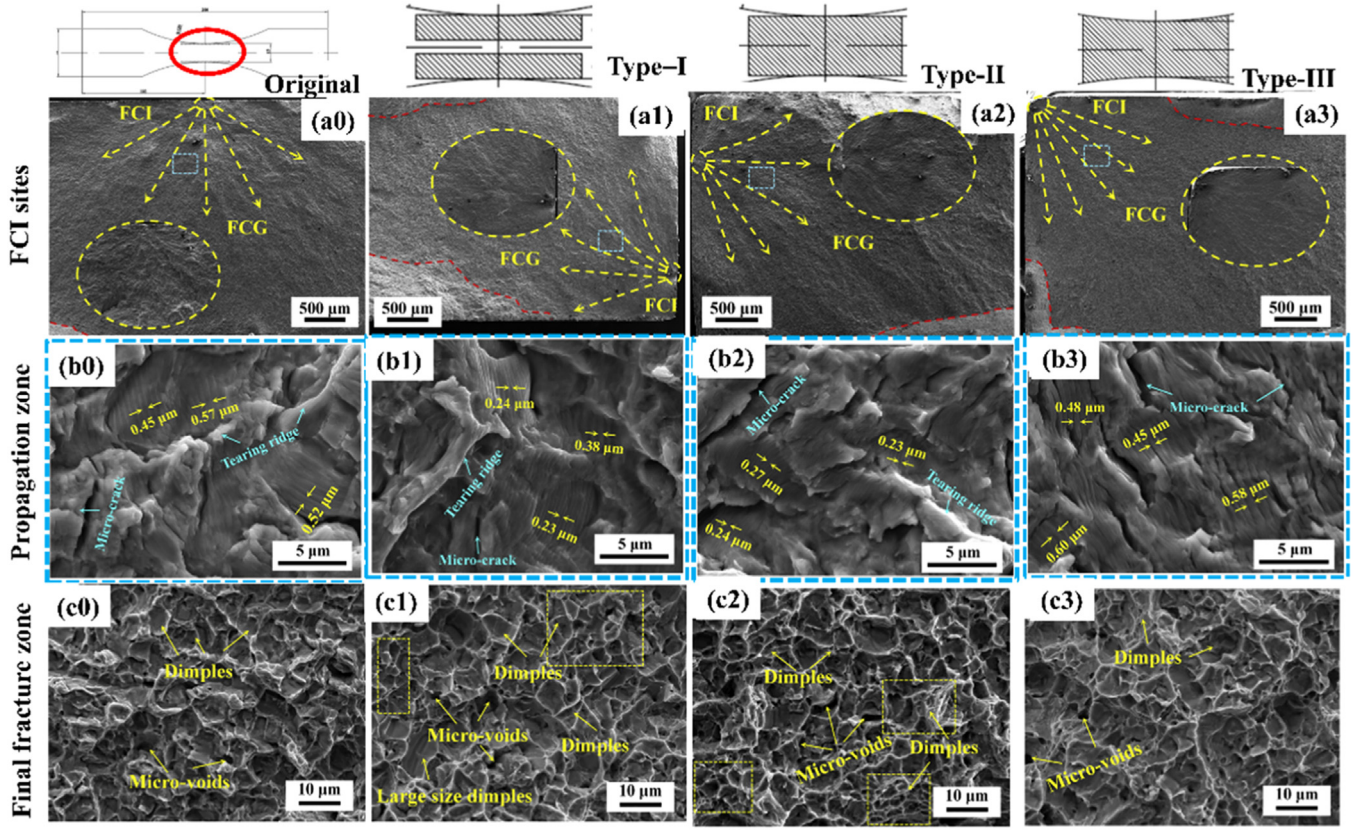

Fig. 30. (a) Fatigue crack initiation sites in different samples, (b) fatigue striations and (c) final fracture zones of the unprocessed and LSP processed samples with different processing parameters. 0, 1, 2, and 3 were referenced as original, Type-I, Type-II and Type-III, respectively. Reproduced from Ref. [60] with permission of the publisher (Elsevier).

corrosion resistance under LSP treatment. Luo et al. [137] studied the corrosion resistance of LSPed Ti80 alloys with equiaxial, bimodal and lamellar initial microstructure. Fig. 32(a–c) shows the different microstructures of Ti80 alloy after LSP. The results showed that LSP can improve the corrosion resistance of three microstructures. This is attributed to the increase of grain boundaries and twin boundaries, which accelerates the formation of passivation film. As shown in the polarization curve (Fig. 32(d, e)), the corrosion potential (E_{corr}) increases and corrosion current density (J_{corr}) decreases for three different initial microstructures after LSP, indicating that the oxide film at the alloy surface becomes denser. Equiaxial and bimodal initial microstructures have weaker corrosion resistance than the other, due to the broader active dissolution zone where Ti matrix oxidizes to Ti^{3+} and dissolves. According to electrochemical impedance spectroscopy analysis, corrosion resistance also can be evaluated by the capacitive resistance (R_p). The R_p of lamellar microstructure was obviously enhanced after LSP than the other two (Fig. 32(f, g)). In conclusion, the corrosion resistance order of LSPed specimen was lamellar > equiaxial > bimodal microstructure. Compared with β phase, the smaller potential in α phase can lead to the corrodes preferentially. Therefore, the greater thickness of the α phase has bad corrosion resistance.

5. Challenge and future research directions

5.1. Current challenges

Since the development of LSP technology, significant progress has been made towards its industrialization and commercialization. With an in-depth understanding of the processing-microstructure-property relationship, LSP has been successfully utilized for enhancing the engineering performance of critical mechanical components in aerospace industry, such as turbine blades, gear shafts, and rotor discs, in which Ti alloys have been widely used [139]. Moreover, the demand for improving the biocompatibility and mechanical properties of Ti alloy implants also drives the investigation of LSP on bio-medical applications [140]. In addition, due to its capability to introduce CRS, LSP has also been deemed as an efficient approach to tailor the residual stress state in some welding joints or additive manufactured parts, by converting the undesirable tensile residual stress to the beneficial CRS [141,142]. However, as Ti alloys have been widely utilized as mechanical components with complex shapes, it is expected that LSP equipment could have the capacity to process the components with high flexibility. Moreover, Ti alloys have been more and more widely applied in a variety of applications in harsh environments, and the demand for further improving the engineering properties of Ti alloys has become an urgent issue. Therefore, several challenges with respect to the flexibility, stability, and homogeneity of LSP remain to be addressed for the LSP of Ti alloys.

(1) Flexibility

With the rapid development of additive manufacturing and advanced welding technology, Ti alloys could be manufactured into quiet complex shapes with concave surfaces or welded with other metallic materials with complicated joint structures. Moreover, LSP is expected to be utilized not only in the production process in factory, but also for field maintenance of existing outdoor structures, such as bridges, ships, airplanes, etc. Therefore, it is necessary to develop mobile LSP equipment with high flexibility, which will also promote the application of LSP industrialization. Additionally, the mobile LSP should equip adjustable laser energy, suitable spot size, high precision, and

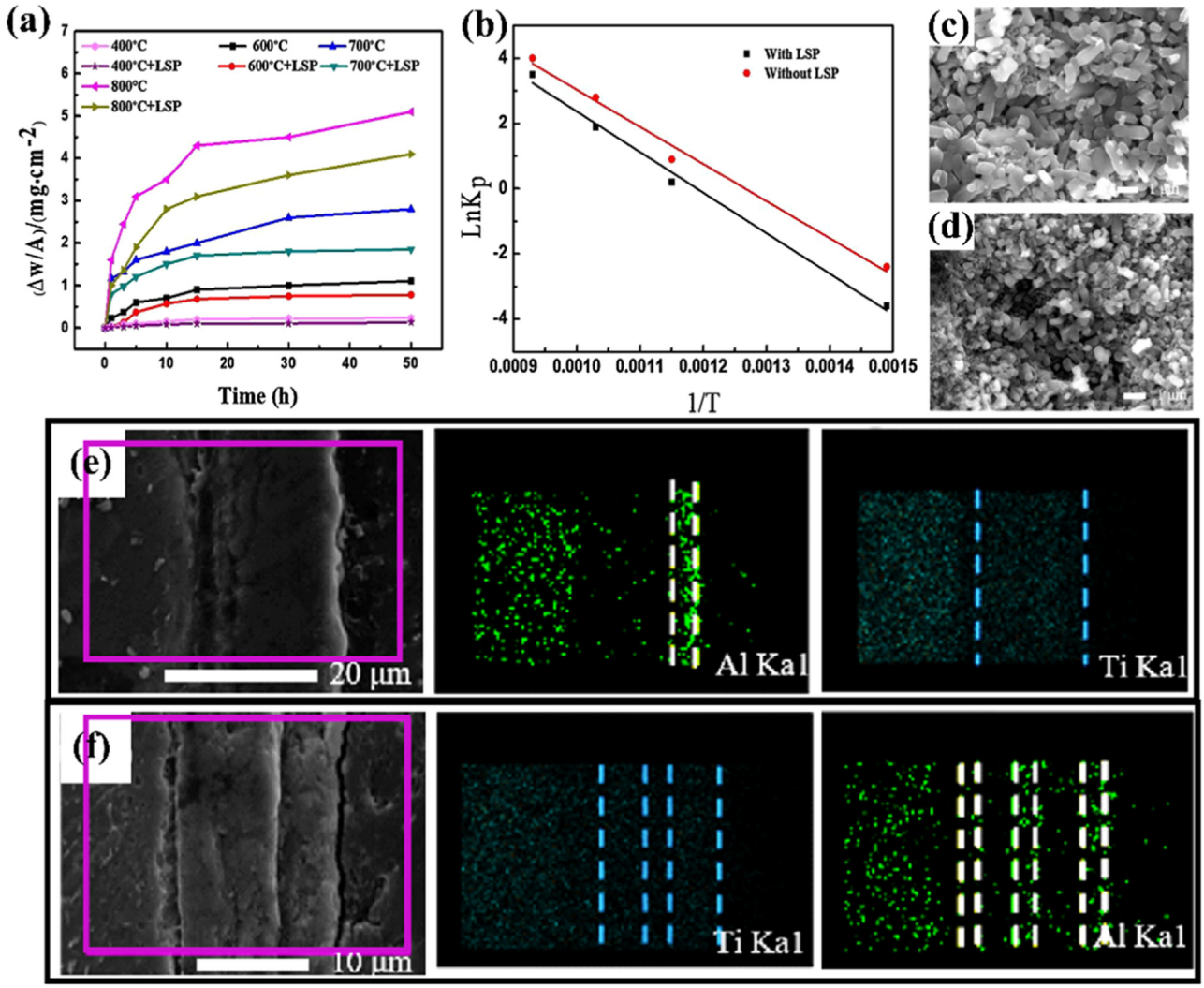

Fig. 31. (a) Isothermal oxidation kinetics graph and (b) activation energy of Ti64 alloy before and after LSP. Microstructures of the oxide layer oxidized at 700 °C: (c) before LSP; (d) after LSP. EDS images denoting the elemental distribution on the scale at the cross section after oxidation at 700 °C for 50 h: (e) before LSP; (f) after LSP. Reproduced from Ref. [138] with permission of the publisher (Elsevier).

high efficiency of laser, so that to overcome different field situations.

(2) Stability
It is well known that the LSP is widely used to enhance the engineering performance of metallic materials by introducing CRS with high magnitude of depth and value. However, as the processed metallic material is subjected to external loading or aging during its operational life, the CRS gradually releases, leading to the deterioration of its engineering properties. Therefore, it is crucial to design novel LSP processes to maintain the introduced CRS and microstructure for the LSPed Ti alloy components.

(3) Homogeneity
LSP has been proved to be an effective approach to improve the fatigue durability of critical structural components of aircraft engine blades which always hold a complex geometry. However, due to the Gaussian distribution of the plasma pressure for a single laser spot and successive overlapping LSP impacts, the whole LSPed surface might be inhomogeneous and thus bring about uneven strengthening effect. Moreover, the inhomogeneous surface plastic deformation will result in increased surface roughness which is undesirable in terms of fatigue life improvement. Therefore, it is of great importance to increase the surface homogeneity of LSPed Ti alloy materials. The gradient dislocation movement induced the formation of a gradient structure, resulting in a distribution of hardness. In order to characterize the microstructure at different depths, metallography, EBSD and TEM are widely used. Moreover, CRS, surface hardness, fatigue life, and corrosion resistance are catching even more attention to evaluate the enhanced engineering performance after LSP. However, how to combine the strengthening of engineering performance after LSP and the microstructure at macro and micro scales becomes a problem.

5.2. Future research directions outlook

Due to the aforementioned challenges, there are still many obstacles hindering the effective utilization of LSP to improve the engineering performance of Ti alloys. To overcome these obstacles, a full understanding of the mechanism of microstructural evolution and enhanced engineering performance of Ti alloys processed by LSP is indispensable. Therefore, future research directions might be carried out in the following discussions to address these critical challenges, which are also illustrated in Fig. 33.

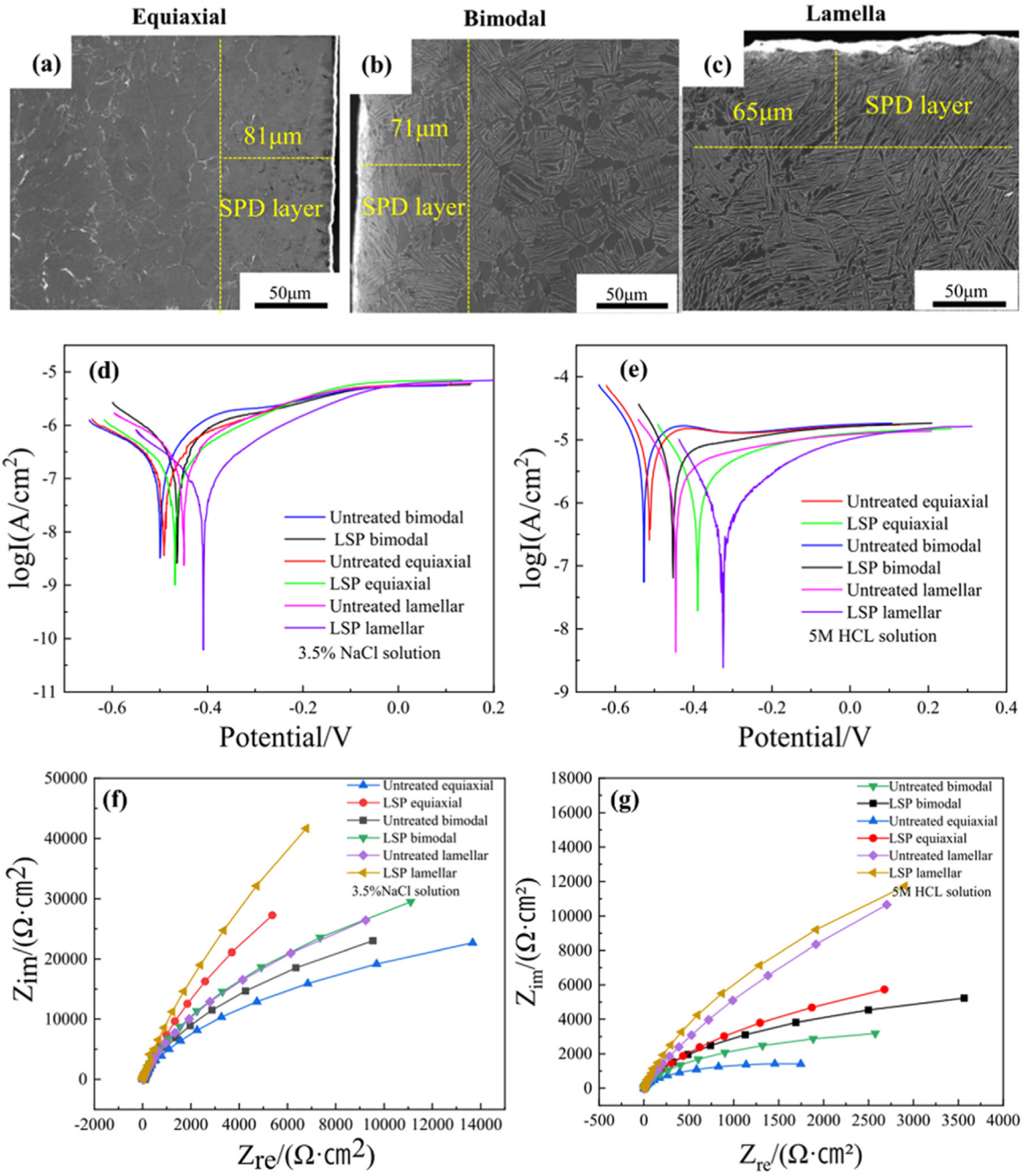

Fig. 32. (a-c) SEM morphology of Ti80 alloy with different microstructure features after LSP. (d, e) Polarization curves and (f, g) electrochemical impedance spectroscopy of Ti80 alloys before and after LSP: (d, f) in 3.5% NaCl solution and (e, g) in 5 mol/L HCL solution, respectively. Reproduced from Ref. [137] with permission of the publisher (Elsevier).

(1) Portable LSP design

With the emergence of compact high-power microchip lasers, the development of a portable LSP facility has become possible and will make a big difference. A compact laser, coupled with a flexible robotic arm, would greatly expand the potential applications of LSP beyond production settings, facilitating the field maintenance of existing outdoor structures such as bridges, ships, and airplanes [143]. When combining the compact laser with drones, these portable LSPs could be utilized for replacing scaffolding and labor in building maintenance operations. Therefore, developing portable LSP equipment is essential, which can greatly broaden the applications of LSP techniques to enhance the engineering performance of Ti alloy components.

(2) LSP integrated with extra processing techniques.

With the rapid development of other advanced material processing techniques, such as ultrasonic, magnetic, and electric field assisted material processing approaches, LSP integrated with these techniques may magnify its effectiveness and have gained more and more attention. Moreover, tailoring the LSP processing temperature could also significantly change the microstructure evolution of CRS distribution of Ti alloy processed. For instance, it has been proved that magnetic-mechanical coupling effect prominently improves the dislocation activities in some metallic materials, which paves a possible way to bring about a more effective processing effect [144]. In order to further improve the circulation stability and thermal stability of the LSPed microstructure and reduce CRS relaxation at high

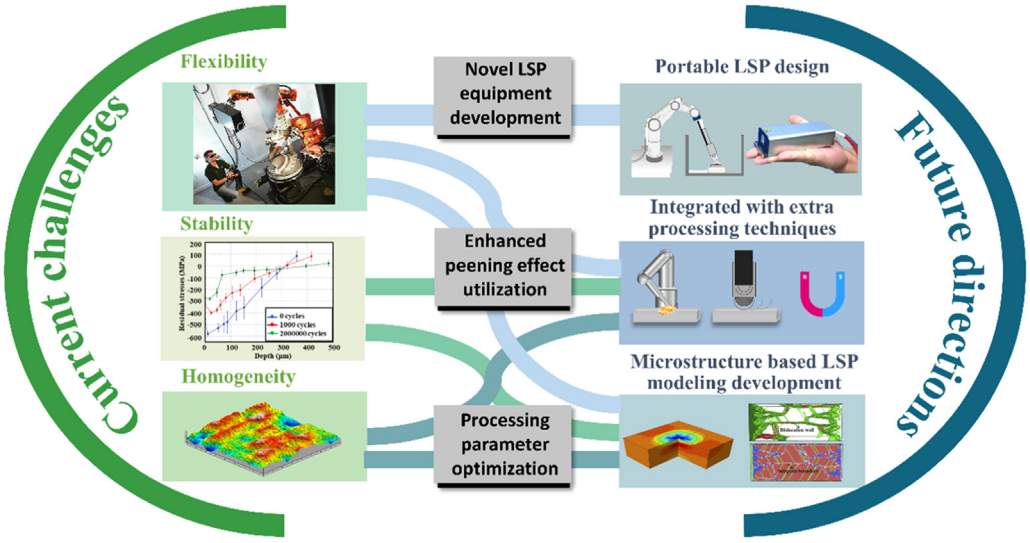

Fig. 33. Summary of current challenges and future research directions of LSP of Ti alloys.

temperatures or under cyclic loading, it is necessary to take advantage of advanced material processing methods (such as magnetic field and ultrasonic vibration) in combination with LSP. The combination of these extra fields has introduced new pathways for the development of LSP technology, generating more possibilities for microstructure tuning and performance optimization of Ti alloys.

(3) Microstructure based LSP modeling development
A thorough understanding of the process-microstructure-performance relationships is of great importance for the processing parameters optimization, and therefore increases the surface homogeneity and integrity of Ti alloy components processed by LSP. However, due to massive processing variables, such as overlapping ratio, laser beam size, etc., and diversity of Ti alloys, exploring the suitable LSP processing conditions for specific Ti alloy components is often costly and time-consuming. Microstructure based LSP modeling and simulation are necessary in order to eliminate trial-and-error loops during the development of LSP process, due to their capability to illustrate complex macrostructural evolution scenarios and to make reliable predictions of the engineering performance.

6. Conclusion

The present work systematically reviews the state-of-the-arts of LSP of Ti alloys. The fundamental mechanisms of LSP principle and design were presented. Some emergent novel LSP techniques with processing at different temperatures or integrated with external fields were discussed. Furthermore, typical microstructural evolution characteristics, including dislocation accumulation, stacking faults evolution, deformation twinning, phase transformation, grain refinement, and surface amorphization, during LSP of Ti alloys were reviewed. The effects of LSP on the engineering performance in terms of surface hardness, wear resistance, fatigue durability, and corrosion resistance of Ti alloys were summarized. The relationships among the microstructural evolution, engineering performance enhancement, and processing parameters of LSPed Ti and its alloys in recent studies are systematically summarized. Moreover, current challenges of applications of LSP to further improve the engineering performance of Ti alloys were discussed and future research directions were put forwarded. It is expected the knowledge gained from this review paper will provide insights and guidance for future LSP processing designs that will result in Ti and its alloys with outstanding engineering performance for a wider range of applications.

Declaration of competing interest

The authors declare that they have no known competing financial interests or personal relationships that could have appeared to influence the work reported in this paper.

CRediT authorship contribution statement

Qian Liu: Conceptualization, Investigation, Methodology, Writing – original draft, Writing – review & editing. **Shuangjie Chu:** Resources, Validation. **Xing Zhang:** Conceptualization, Writing – review & editing. **Yuqian Wang:** Investigation, Project administration, Writing – original draft, Writing – review & editing. **Haiyan Zhao:** Formal analysis, Investigation, Methodology. **Bohao Zhou:** Investigation, Methodology. **Hao Wang:** Data curation, Formal analysis, Resources. **Genbin Wu:** Data curation, Investigation, Methodology. **Bo Mao:** Formal analysis, Funding acquisition, Investigation, Project administration, Supervision, Writing – original draft, Writing – review & editing.

Acknowledgements

This work was financially supported by the National Key R&D Plan of China (No. 2022YFB3705603), the National Natural Science Foundation of China (No. 52101046), the Excellent Youth Overseas Project of National Science and Natural Foundation of China, the Baowu Special Metallurgy Cooperation Limited (No. 22H010101336), and the Medicine-Engineering Interdisciplinary Project of Shanghai Jiao Tong University (No. YG2022QN076).

References

[1] P. Pushp, S.M. Dasharath, C. Arati, Mater. Today-Proc. 54 (2022) 537–542.
[2] J. Chi, Z. Cai, Z. Wan, H. Zhang, Z. Chen, L. Li, Y. Li, P. Peng, W. Guo, Surf. Coat. Technol. 396 (2020) 125908.
[3] M. Peters, J. Kumpfert, C.H. Ward, C. Leyens, Adv. Eng. Mater. 5 (2003) 419–427.
[4] L.J. Wu, K.Y. Luo, Y. Liu, C.Y. Cui, W. Xue, J.Z. Lu, Appl. Surf. Sci. 431 (2018) 122–134.
[5] M. Niinomi, Mater. Sci. Eng. A 243 (1998) 231–236.
[6] R.R. Boyer, JOM 62 (2010) 21–24.
[7] C. Cui, B. Hu, L. Zhao, S. Liu, Mater. Des. 32 (2011) 1684–1691.
[8] Y. Zhao, Mater. China 33 (2014) 698 -404.

[9] Y.Y. Avcu, E. Iakovakis, M. Guney, E. Çalım, A. Özkılınç, E. Abakay, F. Sönmez, F.G. Koç, R. Yamanoğlu, A. Cengiz, E. Avcu, Coatings 13 (2023) 89–108.
[10] H. Lee, S. Mall, S. Sathish, Mater. Sci. Eng. A 390 (2005) 227–232.
[11] A.L. Wen, S.W. Wang, R.M. Ren, X.X. Yan, Adv. Mater. Res. 97–101 (2010) 2217–2220.
[12] P. Kumar, G.S. Mahobia, V. Singh, K. Chattopadhyay, Int. J. Fatigue 166 (2023) 107289.
[13] S. Xu, Y. Cao, B. Duan, H. Liu, J. Wang, C. Si, Surf. Coat. Technol. 458 (2023) 129325.
[14] N. Ao, D. Liu, X. Zhang, S. Wu, Int. J. Fatigue 170 (2023) 107567.
[15] C. Liu, D. Liu, X. Zhang, G. He, X. Xu, N. Ao, A. Ma, D. Liu, Surf. Coat. Technol. 370 (2019) 24–34.
[16] Z. Ren, Z. Li, S. Zhou, Y. Wang, L. Zhang, Z. Zhang, Simul. Model. Pract. Theory 121 (2022) 102643.
[17] H. Su, X. Shen, C. Xu, J. He, B. Wang, G. Su, J. Mater. Res. Technol. 9 (2020) 8172–8185.
[18] S. Jelliti, C. Richard, D. Retraint, T. Roland, M. Chemkhi, C. Demangel, Surf. Coat. Technol. 224 (2013) 82–87.
[19] K.Y. Zhu, A. Vassel, F. Brisset, K. Lu, J. Lu, Acta Mater. 52 (2004) 4101–4110.
[20] S. Singh, K.K. Pandey, V.K. Balla, M. Das, A.K. Keshri, JOM 73 (2021) 4387–4396.
[21] A.K. Gujba, Z. Ren, Y. Dong, C. Ye, M. Medraj, Surf. Coat. Technol. 307 (2016) 157–170.
[22] R. Liu, S. Yuan, N. Lin, Q. Zeng, Z. Wang, Y. Wu, J. Mater. Res. Technol. 11 (2021) 351–377.
[23] A. Amanov, I.-S. Cho, D.-E. Kim, Y.-S. Pyun, Surf. Coat. Technol. 207 (2012) 135–142.
[24] K. Ding, L. Ye, in: Laser Shock Peening: Performance and Process Simulation, Woodhead, New York, 2006, pp. 1–25.
[25] E. Maleki, O. Unal, A. Amanov, Surf. Interfaces 13 (2018) 233–254.
[26] N. Anderholm, Appl. Phys. Lett. 16 (1970) 113–115.
[27] B. Mao, Y. Liao, B. Li, Appl. Surf. Sci. 457 (2018) 342–351.
[28] A.M. Ralls, B. Mao, P.L. Menezes, J. Tribol. 145 (2023) 071702.
[29] A. Siddaiah, B. Mao, Y. Liao, P.L. Menezes, Surf. Coat. Technol. 351 (2018) 188–197.
[30] B. Mao, A. Siddaiah, X. Zhang, B. Li, P.L. Menezes, Y. Liao, Appl. Surf. Sci. 480 (2019) 998–1007.
[31] A. Siddaiah, B. Mao, Y. Liao, P.L. Menezes, J. Tribol. 142 (2020) 041701.
[32] A. Siddaiah, B. Mao, A.K. Kasar, Y. Liao, P.L. Menezes, Wear 462 (2020) 203490.
[33] B. Mao, B. Li, D. Lin, Y. Liao, Mater. Sci. Eng. A 756 (2019) 219–225.
[34] B. Mao, Laser Shock Processing of Magnesium Alloys: Microstructure Evolution and Enhanced Mechanical Properties, Ph.D. Thesis, University of Nevada, Reno, 2020.
[35] Y. Yang, Y. Lu, W. Shi, B. Hou, H. Qiao, J. Qi, E. Zhang, G. Qin, Opt. Laser Technol. 158 (2023) 108794.
[36] B. Wang, L. Cheng, D. Li, Int. J. Fatigue 156 (2022) 106668.
[37] X. Jin, L. Lan, S. Gao, B. He, Y. Rong, Mater. Sci. Eng. A 780 (2020) 139199.
[38] G. Li, S. Chandra, R.A. Rahman Rashid, S. Palanisamy, S. Ding, J. Manuf. Process. 75 (2022) 72–99.
[39] Z.P. Tong, X.D. Ren, W.F. Zhou, S. Adu-Gyamfi, L. Chen, Y.X. Ye, Y.P. Ren, F.Z. Dai, J.D. Yang, L. Li, Opt. Laser Technol. 109 (2019) 139–148.
[40] X.C. Zhang, Y.K. Zhang, J.Z. Lu, F.Z. Xuan, Z.D. Wang, S.T. Tu, Mater. Sci. Eng. A 527 (2010) 3411–3415.
[41] Y. Hua, Y. Bai, Y. Ye, Q. Xue, H. Liu, R. Chen, K. Chen, Appl. Surf. Sci. 283 (2013) 775–780.
[42] H. Zhang, Z. Cai, J. Chi, R. Sun, Z. Che, L. Lin, P. Peng, H. Zhang, W. Guo, Surf. Coat. Technol. 437 (2022) 128378.
[43] X. Luo, N. Dang, X. Wang, Int. J. Fatigue 153 (2021) 106465.
[44] Y. Yang, W. Zhou, B. Chen, Z. Tong, L. Chen, X. Ren, Int. J. Fatigue 136 (2020) 105596.
[45] H. Zhang, Z. Cai, J. Chi, R. Sun, Z. Che, H. Zhang, W. Guo, J. Alloy. Compd. 887 (2021) 161427.
[46] L. Zhou, X. Pan, X. Shi, T. Du, L. Wang, S. Luo, W. He, P. Chen, Vacuum 196 (2022) 110717.
[47] J. Lv, K. Luo, H. Lu, Z. Wang, J. Liu, J. Lu, J. Alloy. Compd. 899 (2022) 163335.
[48] W. Guo, Y. Zhang, H. Sun, H. Zhang, Y. Zhu, Opt. Laser Technol. 158 (2023) 108851.
[49] S. Lou, Y. Li, L. Zhou, X. Nie, G. He, Y. Li, W. He, Mater. Des. 104 (2016) 320–326.
[50] J.Z. Lu, L.J. Wu, G.F. Sun, K.Y. Luo, Y.K. Zhang, J. Cai, C.Y. Cui, X.M. Luo, Acta Mater. 127 (2017) 252–266.
[51] X. Huang, W. Zhu, K. Chen, R.L. Narayan, U. Ramamurty, L. Zhou, W. He, Int. J. Plast. 159 (2022) 103476.
[52] L. Li, W. Jia, V. Ji, Surf. Coat. Technol. 450 (2022) 129010.
[53] C.S. Montross, T. Wei, L. Ye, G. Clark, Yiu-Wing Mai, Int. J. Fatigue 24 (2002) 1021–1036.
[54] W. Deng, C. Wang, H. Lu, X. Meng, Z. Wang, J. Lv, K. Luo, J. Lu, Int. J. Mach. Tool. Manuf. 191 (2023) 104061.
[55] K. Praveenkumar, S. Sudhagara Rajan, S. Swaroop, G. Manivasagam, Surf. Eng. 39 (2023) 245–274.
[56] S. Kalainathan, S. Prabhakaran, Opt. Laser Technol. 81 (2016) 137–144.
[57] Y. Liao, C. Ye, G.J. Cheng, Opt. Laser Technol. 78 (2016) 15–24.
[58] R. Fabbro, P. Peyre, L. Berthe, X. Scherpereel, J. Laser Appl. 10 (1998) 265–279.
[59] P.L.N. Fernando, D. Mohotti, A. Remennikov, P.J. Hazell, H. Wang, A. Amin, Int. J. Mech. Sci. 178 (2020) 3–21.
[60] R. Sun, Z. Che, Z. Cao, S. Zou, J. Wu, W. Guo, Y. Zhu, Surf. Coat. Technol. 383 (2020) 125284.
[61] C. Ye, Y. Liao, G.J. Cheng, Adv. Eng. Mater. 12 (2010) 291–297.
[62] Y. Lu, J. Zhao, H. Qiao, T. Hu, B. Sun, J. Wu, AIP Adv. 9 (2019) 085030.
[63] K. Peng, W. Chen, K. Qian, Mater. Sci. Eng. A 415 (2006) 53–58.
[64] X. Pan, W. He, X. Huang, X. Wang, X. Shi, W. Jia, L. Zhou, Surf. Coat. Technol. 405 (2021) 126670.
[65] J.Z. Zhou, X.K. Meng, S. Huang, J. Sheng, J.Z. Lu, Z.R. Yang, C. Su, Mater. Sci. Eng. A 643 (2015) 86–95.
[66] J. Li, J. Zhou, A. Feng, S. Huang, X. Meng, Y. Sun, Y. Sun, X. Tian, Y. Huang, Mater. Sci. Eng. A 734 (2018) 291–298.
[67] J. Li, J. Zhou, A. Feng, Y. Huang, X. Tian, S. Huang, X. Meng, Opt. Laser Technol. 120 (2019) 105763.
[68] J. Zhou, J. Li, S. Huang, J. Sheng, X. Meng, Q. Sun, Y. Sun, G. Xu, Y. Sun, H. Li, Mater. Sci. Eng. A 718 (2018) 207–215.
[69] C. Ye, S. Suslov, D. Lin, Y. Liao, X. Fei, G.J. Cheng, J. Appl. Phys. 110 (2011) 083504.
[70] J. Li, J. Zhou, L. Liu, A. Feng, S. Huang, X. Meng, Surf. Coat. Technol. 409 (2021) 126848.
[71] W. Zhao, D. Liu, X. Zhang, H. Zhang, J. Liu, C. Ma, R. Zhang, Y. Dong, C. Ye, Surf. Coat. Technol. 397 (2020) 125994.
[72] Y. Sun, H. Liu, Y. Ma, H. Zhang, X. Wang, J. Mater. Eng. Perform. 31 (2022) 6595–6605.
[73] R. Zhu, G. Tang, S. Shi, M. Fu, J. Mater, Process. Technol. 213 (2013) 30–35.
[74] A. Hosoi, T. Nagahama, Y. Ju, Mater. Sci. Eng. A 533 (2012) 38–42.
[75] J. Kuang, X. Li, X. Ye, J. Tang, H. Liu, J. Wang, G. Tang, Metall. Mater. Trans. A 46 (2015) 1789–1804.
[76] J. Kuang, X. Du, X. Li, Y. Yang, A.A. Luo, G. Tang, Scr. Mater. 114 (2016) 151–155.
[77] H. Zhang, Z. Ren, J. Liu, J. Zhao, Z. Liu, D. Lin, R. Zhang, M.J. Graber, N.K. Thomas, Z.D. Kerek, G.-X. Wang, Y. Dong, C. Ye, J. Alloy. Compd. 802 (2019) 573–582.
[78] Z. Wang, W. Zhou, K. Luo, H. Lu, J. Lu, Int. J. Fatigue 172 (2023) 107631.
[79] X. Nie, W. He, L. Zhou, Q. Li, X. Wang, Mater. Sci. Eng. A 594 (2014) 161–167.
[80] G. He, C. Qian, Z. Cai, K. Li, Q. Liu, J. Yan, Adv. Eng. Mater. 25 (2023) 2201843.
[81] G.R. Li, H.-M. Wang, P.-S. Li, L.-Z. Gao, C.-X. Peng, R. Zheng, Acta Phys. Sin 64 (2015) 148102.
[82] F. Ji, W. Deng, H. Lu, L. Wu, K. Luo, J. Lu, Surf. Coat. Technol. 440 (2022) 128513.
[83] C. Wang, L. Wang, C.-L. Wang, K. Li, X.-G. Wang, Opt. Laser Technol. 121 (2020) 105827.
[84] L. Li, W. Jia, V. Ji, Vacuum 206 (2022) 111510.
[85] Z. Tong, X. Ren, Y. Ren, F. Dai, Y. Ye, W. Zhou, L. Chen, Z. Ye, Surf. Coat. Technol. 335 (2018) 32–40.
[86] L. Zhou, Y. Li, W. He, G. He, X. Nie, D. Chen, Z. Lai, Z. An, Mater. Sci. Eng. A 578 (2013) 181–186.
[87] S. Mironov, M. Ozerov, A. Kalinenko, N. Stepanov, O. Plekhov, R. Sikhamov, V. Ventzke, N. Kashaev, G. Salishchev, L. Semiatin, S. Zherebtsov, J. Alloy. Compd. 900 (2022) 163383.
[88] X. Pan, X. Wang, Z. Tian, W. He, X. Shi, P. Chen, L. Zhou, J. Alloy. Compd. 850 (2021) 156672.
[89] J. Lu, H. Lu, X. Xu, J. Yao, J. Cai, K. Luo, Int. J. Mach. Tool. Manuf. 148 (2020) 103475.
[90] W. Jia, Y. Zan, C. Mao, S. Li, W. Zhou, Q. Li, S. Zhang, V. Ji, Vacuum 184 (2021) 109906.
[91] S. Chen, J. Mu, Y. Wang, M. Zhang, Y. Ren, Z. An, Mater. Charact. 159 (2020) 110017.
[92] D. He, L. Li, Y. Zhang, J. Chi, H. Zhang, R. Sun, Z. Che, H. Zhang, W. Guo, J. Alloy. Compd. 935 (2023) 168139.
[93] W. Jia, Q. Hong, H. Zhao, L. Li, D. Han, Mater. Sci. Eng. A 606 (2014) 354–359.
[94] S.J. Lainé, K.M. Knowles, P.J. Doorbar, R.D. Cutts, D. Rugg, Acta Mater. 123 (2017) 350–361.
[95] C. Wang, K. Li, X. Hu, H. Yang, Y. Zhou, Opt. Laser Technol. 142 (2021) 107163.
[96] C. Gu, M. Su, Z. Tian, J. Zhao, Y. Wang, Opt. Laser Technol. 165 (2023) 109629.
[97] A. Bisht, R. Kalsar, A. Adak, I. Dey, K. Jana, A. Lad, G.R. Kumar, G. Jagadeesh, S. Suwas, Acta Mater. 150 (2018) 161–172.
[98] H. Feng, Q.H. Fang, B. Liu, Y. Liu, Y.W. Liu, P.H. Wen, Mech. Mater. 109 (2017) 26–33.
[99] L. Capolungo, I.J. Beyerlein, Phys. Rev. B 78 (2008) 024117.
[100] S. Huang, Y. Zhu, W. Guo, P. Peng, X. Diao, Surf. Coat. Technol. 327 (2017) 32–41.
[101] S. Mironov, M. Ozerov, A. Kalinenko, I. Zuiko, N. Stepanov, O. Plekhov, G. Salishchev, L. Semiatin, S. Zherebtsov, Materials (Basel) 16 (2023) 5365.
[102] J. Jamieson, Science 140 (1963) 72–73.
[103] Y. Guo, B. Jia, Q. Zhou, W. Chen, Y. Ren, R. Liu, A. Arab, C. Ran, P. Chen, Mater. Sci. Eng. A 863 (2023) 144542.
[104] R.G. Hennig, D.R. Trinkle, J. Bouchet, S.G. Srinivasan, R.C. Albers, J.W. Wilkins, Nat. Mater. 4 (2005) 129–133.
[105] H. Zong, X. Ding, T. Lookman, J. Sun, Acta Mater. 115 (2016) 1–9.
[106] X.D. Ren, W.F. Zhou, F.F. Liu, Y.P. Ren, S.Q. Yuan, N.F. Ren, S.D. Xu, T. Yang, Appl. Surf. Sci. 363 (2016) 44–49.
[107] J. Zhao, X. Pan, J. Li, Z. Huang, Q. Kan, G. Kang, L. Zhou, X. Zhang, Int. J. Mech. Sci. 213 (2022) 106874.
[108] J.Z. Lu, H.F. Duan, K.Y. Luo, L.J. Wu, W.W. Deng, J. Cai, J. Alloy. Compd. 698 (2017) 633–642.
[109] C. Ye, S. Suslov, X. Fei, G.J. Cheng, Acta Mater. 59 (2011) 7219–7227.

[110] A. Chattopadhyay, G. Muvvala, S. Sarkar, V. Racherla, A.K. Nath, Opt. Laser Technol. 133 (2021) 106527.
[111] X. Shen, P. Shukla, S. Nath, J. Lawrence, Surf. Coat. Technol. 327 (2017) 101–109.
[112] X. Shi, X. Feng, J. Teng, K. Zhang, L. Zhou, Vacuum 184 (2021) 109986.
[113] K. Yang, Q. Huang, B. Zhong, Q. Wang, Q. Chen, Y. Chen, N. Su, H. Liu, Int. J. Fatigue 141 (2020) 105868.
[114] X. Nie, W. He, S. Zang, X. Wang, J. Zhao, Surf. Coat. Technol. 253 (2014) 68–75.
[115] R. Sun, L. Li, W. Guo, P. Peng, T. Zhai, Z. Che, B. Li, C. Guo, Y. Zhu, Mater. Sci. Eng. A 737 (2018) 94–104.
[116] E. Maawad, Y. Sano, L. Wagner, H.G. Brokmeier, C. Genzel, Mater. Sci. Eng. A 536 (2012) 82–91.
[117] Z. Cao, H. Xu, S. Zou, Z. Che, Chin. J. Aeronaut. 25 (2012) 650–656.
[118] X. Shen, P. Shukla, A.K. Subramaniyan, A. Zammit, P. Swanson, J. Lawrence, M.E. Fitzpatrick, Opt. Laser Technol. 131 (2020) 106446.
[119] C. Cellard, D. Retraint, M. François, E. Rouhaud, D.Le Saunier, Mater. Sci. Eng. A 532 (2012) 362–372.
[120] P. Luo, D.T. McDonald, W. Xu, S. Palanisamy, M.S. Dargusch, K. Xia, Scr. Mater. 66 (2012) 785–788.
[121] B.J. Hayes, B.W. Martin, B. Welk, S.J. Kuhr, T.K. Ales, D.A. Brice, I. Ghamarian, A.H. Baker, C.V. Haden, D.G. Harlow, H.L. Fraser, P.C. Collins, Acta Mater. 133 (2017) 120–133.
[122] S. Petronić, K. Čolić, B. Đorđević, D. Milovanović, M. Burzić, F. Vučetić, Opt. Laser. Eng. 129 (2020) 106052.
[123] N. Maharjan, T. Ramesh, Z. Wang, Appl. Surf. Sci. 638 (2023) 158110.
[124] K. Praveenkumar, S. Swaroop, G. Manivasagam, Opt. Laser Technol. 164 (2023) 109398.
[125] M. Yin, Z. Cai, Z. Li, Z. Zhou, W. Wang, W. He, Trans. Nonferr. Met. Soc. China 29 (2019) 1439–1448.
[126] R. Xin, L. Lan, C. Bai, S. Gao, B. He, J. Wang, J. Mater. Sci. 57 (2022) 9619–9630.
[127] M.H. El Haddad, K.N. Smith, T.H. Topper, J. Eng. Mater. Technol. 101 (1979) 42–46.
[128] Y. Murakami, T. Takagi, K. Wada, H. Matsunaga, Int. J. Fatigue 146 (2021) 106138.
[129] Q. Jiang, S. Li, C. Zhou, B. Zhang, Y. Zhang, Opt. Laser Technol. 144 (2021) 107391.
[130] X. Pan, X. Li, L. Zhou, X. Feng, S. Luo, W. He, Materials 12 (2019) 3799.
[131] K. Praveenkumar, P. Mylavarapu, S. Swaroop, J. Mater. Eng. Perform. 32 (2022) 7348–7362.
[132] R. Sun, L. Li, Y. Zhu, P. Peng, Q. Li, W. Guo, Opt. Laser Technol. 115 (2019) 166–170.
[133] S.A. Mantri, T. Alam, Y. Zheng, J.C. Williams, R. Banerjee, Addit. Manuf. 32 (2020) 101067.
[134] M.R. Akbarpour, S.Moniri Javadhesari, J. Alloy. Compd. 699 (2017) 882–886.
[135] H. Lu, Z. Wang, J. Cai, X. Xu, K. Luo, L. Wu, J. Lu, Corros. Sci. 188 (2021) 109558.
[136] Y. Geng, X. Mei, K. Wang, X. Dong, X. Yan, Z. Fan, W. Duan, W. Wang, J. Mater. Eng. Perform. 27 (2018) 4703–4713.
[137] G. Luo, L. Zhang, Y. Xiong, B. Zhang, X. Chen, Y. Wu, S. Wang, W. Cao, Surf. Coat. Technol. 440 (2022) 128425.
[138] W. Guo, H. Wang, P. Peng, B. Song, H. Zhang, T. Shao, H. Huan, H. Qiao, G. Qu, D. Zhu, J. Yan, Corros. Sci. 170 (2020) 108655.
[139] J. Wu, J. Zhao, H. Qiao, Y. Lu, B. Sun, T. Hu, Y. Zhang, Opto-Electron. Eng. 45 (2018) 170690.
[140] S.R. Mannava, G. Ivetic, S. Bhamare, V. Chaswal, L. Felon, D. Kirschman, D. Lahrman, R. Tenaglia, D. Qian, V. Vasudevan, Int. J. Struct. Integr. 2 (2011) 101–113.
[141] X. Huang, Z. Cao, M. Chang, S. Zou, China Mech. Eng. 29 (2018) 104–109.
[142] Z. Tian, W. He, L. Zhou, Y. Wang, S. Luo, N. Jiang, L. Zhang, Surf. Technol. 51 (2022) 30–37.
[143] Y. Sano, T. Kato, Y. Mizuta, S. Tamaki, K. Yokofujita, T. Taira, T. Hosokai, Y. Sakino, Forces Mech. 7 (2022) 100080.
[144] A.K. Soika, I.O. Sologub, V.G. Shepelevich, P.A. Sivtsova, Phys. Solid State 57 (2015) 1997–1999.